

<sup>1</sup> **An optimal XBT-based monitoring system for the South Atlantic**  
<sup>2</sup> **Meridional Overturning Circulation at 34°S**

Marlos Goes,<sup>1,2</sup> Gustavo Goni,<sup>2</sup> and Shenfu Dong<sup>1,2</sup>

---

Corresponding author: Marlos Goes, CIMAS/University of Miami and NOAA/AOML, Miami, USA. (marlos.goes@noaa.gov)

<sup>1</sup>CIMAS, University of Miami, Miami, FL, USA.

<sup>2</sup>PHOD, NOAA/AOML, Miami, FL, USA.

3 **Abstract.** The South Atlantic is an important pathway for the inter-basin  
4 exchanges of heat and freshwater with strong influence on the global merid-  
5 ional overturning stability and variability. Along the 34°S parallel, a quar-  
6 terly, high resolution XBT transect (AX18) samples the temperature struc-  
7 ture in the upper ocean. The AX18 transect has been shown to be a useful  
8 component of a meridional overturning monitoring system of the region. How-  
9 ever, a feasible, cost-effective design for an XBT-based system has not yet  
10 been developed. Here we use a high-resolution ocean assimilation product  
11 to simulate an XBT-based observational system across the South Atlantic.  
12 The sensitivity of the meridional heat transport, meridional overturning cir-  
13 culation, and geostrophic velocities to key observational and methodologi-  
14 cal assumptions is studied. Key assumptions taken into account are horizon-  
15 tal and temporal sampling of the transect, salinity and deep temperature in-  
16 ference, as well as the level of reference for geostrophic velocities. With the  
17 current sampling strategy, the largest errors in the meridional overturning  
18 and heat transport estimations are the reference velocity for geostrophic cal-  
19 culations and the western boundary resolution. We use the results obtained  
20 by the state estimation under observational assumptions to make recommen-  
21 dations for potential improvements in the AX18 transect implementation.

## 1. Introduction

22 The Atlantic Ocean circulation is well known for having a deep convection site at high  
23 latitudes in the northern hemisphere, which drives to a large extent the Atlantic meridional  
24 overturning circulation (AMOC) and, therefore, the northward heat transport to the  
25 northern latitudes [*Marshall and Schott, 1999*]. The variability of the AMOC is partly  
26 responsible for changes in the northern hemisphere climate, such as the North Atlantic  
27 storm tracks [*Woollings et al., 2012*] and the North American and European precipitation  
28 patterns [*Enfield et al., 2001; Sutton and Hodson, 2005*], sea level variability [*Levermann*  
29 *et al., 2005; Hu et al., 2011*], uptake of ocean tracers such as CO<sub>2</sub> [*Sabine et al., 2004;*  
30 *Goes et al., 2010*], tropical precipitation [*Zhang and Delworth, 2006*] and El Niño patterns  
31 [*Dong and Sutton, 2007; Timmermann et al., 2007*].

32 Despite the fact that the AMOC strength and variability are highly determined by  
33 changes within the North Atlantic Subpolar gyre [*Hatun et al., 2005; Lohmann et al.,*  
34 *2009*], the deep convection regions between the Greenland-Iceland-Scotland seas are highly  
35 sensitive to heat and freshwater transported from the South Atlantic [*Rahmstorf, 1996;*  
36 *Donners and Drijfhout, 2004*], which is suggested to be one of the main drivers of two  
37 stable states of the AMOC [*Weijer et al., 1999; Beal et al., 2011; Hawkings et al., 2011;*  
38 *Garzoli et al., 2013*].

39 The South Atlantic is an important pathway for exchange of heat and water masses  
40 from other basins through, for example, the Agulhas current region [*Goni et al., 1997*]  
41 and the Brazil-Malvinas confluence region [*Gordon, 1986; Wainer et al., 2000; Goni and*  
42 *Wainer, 2001; Goni et al., 2011*]. The South Atlantic Ocean has been historically one

43 of the least observed regions on the globe; however, several efforts to measure long-term  
44 variability in the basin have been put forward in the last decade. For instance, expendable  
45 bathythermograph (XBT) observations from the high-density XBT transect AX18 (Figure  
46 1a) measures temperature in the upper 800 m of the ocean four times a year along 34°S.  
47 Studies based on the AX18 XBT data have shown that the mean strength of AMOC and  
48 heat transport at 34°S are mostly geostrophically driven, although the seasonal variability  
49 of the meridional transports are equally determined by the geostrophic and the wind-  
50 driven Ekman components [*Dong et al.*, 2009]. The compensation between the Ekman  
51 and geostrophic components may translate into a small annual cycle of heat and volume  
52 transports [*Garzoli and Baringer*, 2007; *Dong et al.*, 2009], although models generally do  
53 not reproduce this characteristic [*Dong et al.*, 2011a].

54 Currently, observational estimates rely on several assumptions to estimate the integral  
55 flow in the South Atlantic. Thus far, only *Baringer and Garzoli* [2007] have estimated the  
56 uncertainty resulting from the underlying XBT-based observational system methodologi-  
57 cal assumptions to measure heat transport across 34°S. However, no sensitivity tests have  
58 yet been performed to derive an optimal AX18 sampling strategy, i.e., a feasible strategy  
59 that maximizes the information content in a cost-effective manner, and to assess the un-  
60 certainty in volume and heat transports associated with observational and computational  
61 methodologies across 34°S. To accomplish this, current high resolution ocean reanalyses  
62 can be useful to assess and investigate potential improvements in the sampling strategy  
63 of the AX18 transect. Similar methodologies have been applied, for example, in several  
64 studies in the North Atlantic [e.g. *Hirschi et al.*, 2003; *Baehr et al.*, 2004, 2008] to evaluate  
65 strategies for monitoring the MOC in the North Atlantic.

66 The aim of the present study is to assess how observational and computational method-  
67 ologies affect the estimates of volume and heat transports across 34°S in Atlantic Ocean,  
68 and how to optimize the design of the AX18 XBT transect in order to reduce uncertainty  
69 estimates. Therefore, this study will address four main objectives to evaluate the AX18  
70 XBT transect:

- 71 i) The optimal spatial (longitudinal) resolution.
- 72 ii) The optimal temporal sampling to capture the seasonal variability of the AMOC in  
73 the region.
- 74 iii) The uncertainties derived from the salinity and deep temperature estimation.
- 75 iv) Potential improvements to the assumptions made regarding the level of reference to  
76 resolve the barotropic mode.

77 To address these goals, we will first describe the characteristics of the region of study  
78 (Section 2). We will use a high-resolution global assimilation model (Section 3) that  
79 compares reasonably well with the regional observations and characteristics presented in  
80 Section 2. We will define the methodology (Section 4) to calculate volume and meridional  
81 heat transport (MHT) across 34°S, and perform controlled experiments in the model  
82 framework to answer point-by-point the above questions (Section 5). Finally, we will  
83 discuss the results and make recommendations for the improvement of the AX18 XBT  
84 transect measurements (Section 6).

## 2. Regional characteristics

85 The subtropical South Atlantic is characterized by a large scale anticyclonic feature,  
86 the South Atlantic subtropical gyre [*Stramma and England, 1999; Garzoli and Matano,*  
87 *2011*]. In the southwestern Atlantic, the surface dynamics are dominated by the Brazil-

88 Malvinas Confluence, which is characterized by the cold northward flow of the Malvinas  
89 Current, and a southward flowing warm weak western boundary current, the Brazil Cur-  
90 rent [Garzoli, 1993]. This region exhibits complex frontal motions [Goni *et al.*, 2011;  
91 Goni and Wainer, 2001] and patterns with the simultaneous presence of warm and cold  
92 rings and eddies [Lentini *et al.*, 2006] and, therefore, it is characterized by large values  
93 of eddy kinetic energy (Figure 1a). In the southeastern Atlantic, the transfer of warm  
94 waters from the Indian Ocean into the South Atlantic subtropical gyre largely takes place  
95 in the form of rings and filaments formed when the Agulhas Current retroflects south of  
96 Africa between 1°W and 25°E [Richardson and Garzoli, 2003; Goni *et al.*, 1997]. The  
97 eastward flowing South Atlantic Current and the northward flowing Benguela Current  
98 delimit the southern and eastern boundaries of the subtropical gyre, respectively. The  
99 Brazil-Malvinas Confluence region and the Agulhas retroflection region represent the most  
100 energetic areas contained in the South Atlantic. These two regions present similar values  
101 of mean eddy kinetic energy, above 1000 cm<sup>2</sup> s<sup>-2</sup> (Figure 1a), as observed by altimetric sea  
102 level anomalies [Ducet *et al.*, 2000] for the 2007-2012 time period. The Brazil-Malvinas  
103 Confluence and Agulhas retroflection regions are both crossed by the XBT transect AX18  
104 (Figure 1a).

### 3. The HYCOM-NCODA reanalysis

105 As suggested in previous studies, the strong mesoscale energy in the South Atlantic re-  
106 gion requires a minimum of eddy-permitting models to resolve its main features [Treguier  
107 *et al.*, 2007; Biastoch *et al.*, 2009]. In the present study we use data from the Hybrid Coor-  
108 dinate Ocean Model (HYCOM)-Navy Coupled Ocean Data Assimilation (NCODA) assim-  
109 ilative product [Chassignet *et al.*, 2009], encompassing a total of nearly 6 years of model

110 simulation, sampled in a 7-day timestep using 7-day averages. We combine three experi-  
111 ments, numbered as GLBa0.08/74.2 (June 2007 to September 2008), GLBa0.08/expt\_90.6  
112 (September 2008 to May 2009), and GLBa0.08/expt\_90.8 (May 2009 to May 2013) in order  
113 to maximize the temporal coverage of the model output.

114 The HYCOM-NCODA is configured for the global ocean with HYCOM 2.2 as the dy-  
115 namical model. Computations are carried out on a Mercator grid between 78°S and 47°N,  
116 with an average of 1/12° ( $\sim 7$  km) horizontal spacing and 32 vertical layers. A bipolar  
117 patch is used for regions north of 47°N. Bathymetry is derived from the U. S. Naval Re-  
118 search Laboratory 2-minute DBDB2 (Digital Bathymetric Data Base) dataset. Surface  
119 forcing is from the Navy Operational Global Atmospheric Prediction System (NOGAPS)  
120 and includes 3-hourly and 0.5° wind stress, wind speed, heat flux (using bulk formula),  
121 and precipitation. The NCODA methodology [Cummings, 2005] uses the model forecast  
122 as a first guess in a multi-variate Optimal Interpolation (MVOI) scheme and assimi-  
123 lates available along-track satellite sea height anomaly observations (obtained via the  
124 Naval Oceanographic Office's Altimeter Data Fusion Center), in-situ sea surface temper-  
125 ature (SST), as well as available in-situ vertical temperature and salinity profiles from  
126 XBTs, ARGO floats and moored buoys. The Modular Ocean Data Assimilation Sys-  
127 tem (MODAS) synthetic profiles are used by NCODA for downward projection of surface  
128 information [Fox et al., 2002].

129 Compared to altimetric observations, the eddy-resolving HYCOM-NCODA reanalysis  
130 reproduces reasonably the main circulation features of the region (Figure 1b). The output  
131 of this model, however, shows lower energy in the high EKE regions such as the Brazil-  
132 Malvinas Confluence and Agulhas retroreflection regions, and higher energy in the low EKE

133 regions (Figure 1c). The negative energy biases are also observed in the comparison of the  
134 sea level root-mean square variability of the AX18 transect boundaries (Figure 2a, b, c).  
135 We select 18 realizations (Figure 2a) of the AX18 transect based on the criteria of being  
136 zonally directed (median angle  $< 10^\circ$ , and with the mean section between  $30^\circ$  and  $36^\circ$  of  
137 latitude) to compare the model thermohaline behavior with the actual XBT observations  
138 along the nominal  $34^\circ\text{S}$ . Below 850 m, the maximum depth sampled by the XBTs, the  
139 WOA05 annual climatology [*Locarnini et al.*, 2006] is used. The mean temperature section  
140 retrieved by the AX18 along the nominal of  $34^\circ\text{S}$  shows an east-west gradient, with higher  
141 upper ocean temperatures in the west (Figure 2d). The associated zonal density gradients  
142 allow average geostrophic volume and heat transports to the north, as shown in previous  
143 studies [e.g., *Ganachaud and Wunsch*, 2003; *Garzoli and Baringer*, 2007]. The model  
144 shows generally negative temperature biases in the interior (1 to  $2^\circ\text{C}$  on average), which  
145 indicates stronger stratification and shoaling of isothermal layers, and positive biases  
146 on the boundaries (1 to  $1.5^\circ\text{C}$  on average) relative to the mean AX18 section above 850  
147 m, and stronger ocean bottom stratification in comparison to the WOA05 climatology  
148 (Figure 2g-i).

#### 4. Methodology

149 This study focuses on the reconstruction of the AMOC streamfunction ( $\Psi_y$ ) and the heat  
150 transport (MHT) along  $34^\circ\text{S}$  by simulating XBT observations in the model framework. For  
151 this, we will use the temperature, salinity and velocity outputs of the model, distributed  
152 over depth and longitude along the  $34^\circ\text{S}$ . This section describes how the AMOC and MHT  
153 are defined through the paper.



## 4.1. AMOC

The AMOC streamfunction is defined as:

$$\Psi_y(z) = \int_{x_E}^{x_W} \int_z^{-H} v(x, z) dx dz \quad (1)$$

i.e., the integral of the meridional velocity  $v(x, z)$  from the bottom ( $H$ ) to the depth ( $z$ ) of the ocean and between the western ( $x_W$ ) and the eastern ( $x_E$ ) boundaries of the basin. The meridional velocity  $v(x, z)$ , and therefore its derived meridional streamfunction, can be decomposed into three dynamical components [Lee and Marotzke, 1998]:

$$v(x, z) = v_{sh}(x, z) + v_{bar}(x) + v_E(x, z) \quad (2)$$

where  $v_{sh}$  is the vertical shear component, which consists of the velocities calculated using the thermal wind relationship, minus a depth independent velocity:

$$v_{sh}(x, z) = \frac{g}{\rho_0 f} \frac{\partial \rho}{\partial x} - \frac{1}{H} \int_{-H}^0 v_{sh}(x, z) dz, \quad (3)$$

the depth independent velocity is known as the barotropic or gyre component  $v_{bar}$ , and is here defined as the local average of  $v(x, z)$  over the depth  $H$  of the ocean:

$$v_{bar}(x) = \frac{1}{H} \int_{-H}^0 v(x, z) dz \quad (4)$$

and the last term  $v_E(x, z)$  is the Ekman component, derived from the local zonal wind stress ( $\tau_x$ ), compensated by a depth-independent flow underneath the Ekman layer:

$$v_E = -\frac{\tau_x}{\rho_0 f D_E} - \frac{1}{H} \int_{-H}^0 v_E(x, z) dz \quad (5)$$

Therefore the Ekman velocity assumes only two different values in the water column, one in the Ekman layer, and another below the Ekman layer [Baehr et al., 2004]. Other ageostrophic contributions rather than Ekman (frictional and non-linear) are not defined.

The constant parameters used here are the mean water density  $\rho_0 = 1025 \text{ kg m}^{-3}$ , the

Coriolis parameter  $f$ , and the depth of the Ekman layer  $D_E$ , which is arbitrarily assumed here to be  $D_E = 50$  m [e.g., *Pond and Pickard*, 1983]. The barotropic and vertical shear velocities combined constitute the absolute geostrophic velocity, which is estimated using the dynamic method assuming a reference level [*Pond and Pickard*, 1983]. Barotropic velocities have a strong contribution to the geostrophic flow at locations of sloping topography, and their projection on the AMOC can therefore be an important term in the AMOC reconstruction [*Baehr et al.*, 2004]. To ensure zero mass transport, a correction is applied to the three components of the meridional velocity by subtracting a spatially constant term proportional to the weighted mean velocity across the section:

$$v(x, z) = v(x, z) - \frac{M_y}{\int_{-H}^0 \int_{x_E}^{x_W} dx dz}, \quad \text{for } M_y = \int_{-H}^0 \int_{x_E}^{x_W} v(x, z) dx dz \quad (6)$$

154 The AMOC strength (in Sv) is further defined as the value of the maximum amplitude  
 155 of the AMOC streamfunction (Equation 1). Since the total velocity is decomposed into  
 156 its physical components in Equation 2, an AMOC strength can also be defined for the  
 157 individual components of the AMOC.

## 4.2. Meridional Heat Transport

The meridional heat transport is calculated as follows:

$$MHT = \rho_0 c_p \int_{-H}^0 \int_{x_E}^{x_W} v(x, z) \theta(x, z) dx dz - \rho_0 c_p M_y \langle \theta \rangle \quad (7)$$

158 where  $c_p = 4187$  J kg<sup>-1</sup>K<sup>-1</sup> is the specific heat of sea water, and  $\langle \theta \rangle$  is the averaged  
 159 potential temperature  $\theta$  along the section. The last term in Equation 7 is a constraint  
 160 to allow zero mass transport across the section, which is necessary for heat transport  
 161 calculations in free surface models, since they do not necessarily have zero mass transport  
 162 at any given time period [*Jayne and Marotzke*, 2001; *Griffies et al.*, 2004].

To reconstruct MHT, Equation 7 is further decomposed into the same components as the meridional overturning, i.e., vertical shear, barotropic and Ekman, respectively, using the corresponding decomposition of the velocity (Equation 2). Following *Hall and Bryden* [1982]:

$$MHT = \rho_0 c_p \int_{-H}^0 \int_{x_E}^{x_W} \{v_{vs}[\theta - \theta_{bar}] + v_{bar}\theta_{bar} + v_{Ek}\theta_{Ek}\} dx dz \quad (8)$$

163 where  $\theta_{bar}$  is the depth-averaged potential temperature, and  $\theta_{ek}$  follows the Ekman velocity  
 164 definition, i.e.,  $\theta_{ek}$  assumes only two values over depth, one as the average in the Ekman  
 165 layer, and another in the layer below the Ekman layer. Each of the terms in Equation  
 166 8 is meaningful as a heat transport, because the velocity components are design to be  
 167 compensated and allow zero net volume transport across the section [*Hirschi et al.*, 2003].  
 168 Therefore, in the reconstruction, the last term in Equation 7 is not necessary. Otherwise,  
 169 the calculated heat transport would be dependent on an arbitrary temperature reference  
 170 [*Montgomery*, 1974].

## 5. Results

### 5.1. AMOC streamfunction reconstruction

171 The AMOC strength calculated from the model output velocities in a 7-day average is  
 172 highly variable in time (Figure 3a; black line), with amplitude ranging from -8 to 35 Sv (1  
 173 Sv =  $10^6 \text{ m}^3\text{s}^{-1}$ ), and with strong high frequency variability as well as a defined annual  
 174 cycle. The time-averaged AMOC streamfunction (Figure 3c) shows positive (northward)  
 175 values in the upper 3500 m, negative (southward) values underneath, and a pronounced  
 176 maximum at the depth of  $\sim 1500$  m, which characterizes the AMOC strength. The time-  
 177 mean AMOC strength in the model is  $15.1 \pm 7.6$  Sv, lower than observational estimates

178 of  $17.9 \pm 2.2$  Sv [Dong *et al.*, 2009], but within the uncertainty estimates. Results from  
179 other high resolution models, e.g. [Dong *et al.*, 2011a] using the OFES model, show a  
180 strong agreement with the AMOC strength value ( $15.0 \pm 3.7$  Sv) presented here.

181 We decompose the AMOC streamfunction into its vertical shear, Ekman, and barotropic  
182 components using the methodology described in Section 44.1. Therefore, each component  
183 is independently estimated, accordingly to Lee and Marotzke [1998] and Baehr *et al.*  
184 [2004], but differently from the methodologies of Perez *et al.* [2011] and Dong *et al.* [2011a],  
185 which estimate the geostrophic transport either unbalanced for mass transport or as the  
186 residual between the total and Ekman transports. The absolute geostrophic component  
187 (barotropic plus vertical shear) is calculated by using a level of known motion at the  
188 bottom of the ocean, assuming that velocities are perfectly known there. Individually,  
189 the vertical shear component has the strongest contribution to the mean AMOC strength  
190 (Figure 3b), with an average of  $26.9 \pm 3.1$  Sv, and it is in great part compensated by the  
191 barotropic contribution of the transport, which is negative (southward) with an average  
192 of  $-15.9 \pm 6$  Sv. The resulting absolute geostrophic transport is  $11 \pm 6.7$  Sv, smaller than  
193 the observational value of  $15.7 \pm 2.6$  Sv [Dong *et al.*, 2009] and that obtained from the  
194 OFES model ( $12.9 \pm 2.1$  Sv; Dong *et al.* [2011a]). It is worth mentioning that neither the  
195 barotropic nor the vertical shear streamfunctions show a reversal in depth, as observed  
196 on the total mean streamfunction, but that the addition of these two streamfunctions  
197 produces the same reversal pattern at approximately 3500 m (magenta line in Figure  
198 3c) as observed in the original model streamfunction. Strong interannual variability is  
199 observed in the barotropic component, with positive anomalies in the austral summer of  
200 2007 and 2008 and negative anomalies in the austral spring of 2009 and 2010. The Ekman

201 component has the lowest contribution to the mean AMOC strength, only  $2 \pm 4$  Sv, but  
202 its maximum amplitude (variability) can reach over 10 Sv, which is stronger than the  
203 other components.

204 The MHT follows the same pattern as the AMOC (Figure 4). The mean MHT calculated  
205 directly from the model fields is  $0.33 \pm 0.5$  PW (1 PetaWatt =  $10^{15}$ W), which is also lower  
206 than the values calculated from observational studies ( $0.54 \pm 0.14$  PW; *Garzoli et al.*  
207 [2013]). The barotropic MHT component ( $-0.6 \pm 0.23$  PW) compensates to a large extent  
208 the vertical shear component ( $0.8 \pm 0.35$  PW), and the Ekman component contributes  
209 about one third of the total MHT ( $0.12 \pm 0.24$  PW).

210 The annual variability of the AMOC and MHT components (Figure 5) shows that  
211 the vertical shear component does not have a noticeable annual cycle. The Ekman and  
212 barotropic components have stronger annual cycles, and are approximately in phase with  
213 each other, with more positive/less negative values from March to August. Therefore,  
214 the total geostrophic transport (vertical shear plus barotropic) and the Ekman compo-  
215 nents have similar phases, a result that is at odds with previous observational studies  
216 [e.g., *Dong et al.*, 2009] that show an out-of-phase relationship between the Ekman and  
217 geostrophic AMOC annual cycle, which produces a much reduced annual cycle of the  
218 AMOC variability. However, other high-resolution models also show a similar annual  
219 cycle for the total AMOC [e.g., *Dong et al.*, 2011a; *Perez et al.*, 2011] as observed here.  
220 The residual contribution, which is the part of the annual variance that is not explained  
221 by the reconstruction (cyan line, Figure 5), is negligible for the AMOC but can reach up  
222 to 0.5 PW for the MHT, especially during the austral summer. As observed in Figure  
223 4a, the MHT calculated directly from the model velocities is weak or sometimes negative

224 during austral summer, but these reversals of MHT are not featured in the reconstruction  
225 (Figure 4a, magenta line). These differences may arise because the model velocities con-  
226 tain ageostrophic terms other than Ekman [*Sime et al.*, 2006], non-linearities in the MHT  
227 calculation, and unbalanced flow of volume ( $0.94 \pm 3.8$  Sv), whose MHT contribution  
228 is here estimated at  $-0.02 \pm 0.06$  PW (Equation 8), the same mean magnitude of 0.02  
229 PW estimated in *Baringer and Garzoli* [2007]. Other methodologies also show a stronger  
230 reconstructed MHT in comparison with the direct estimates from models [*Perez et al.*,  
231 2011]. Surprisingly, the mean of the reconstructed MHT, which is higher than the original  
232 timeseries, is  $0.54 \pm 0.34$  PW, the same value as estimated by *Garzoli and Baringer* [2007]  
233 and *Garzoli et al.* [2013] using XBT observations.

## 5.2. XBT observational strategy

234 The AX18 XBT transect, which was designed with the main purpose of monitoring the  
235 variability of the upper limb of the AMOC transport, measures temperature in the upper  
236 ocean between Cape Town and South America quarterly, with a high-density (between  
237 25-50 km) zonal spacing.

238 Observational studies that used AX18 data to estimate meridional volume and heat  
239 transports involved several methodological assumptions. The XBTs measure tempera-  
240 ture profiles in the upper 800 m depth (e.g. Deep Blue probe type). Because XBTs do  
241 not measure salinity, a common method to infer salinity profiles at an XBT deployment  
242 location uses a lookup table derived from historical temperature-salinity (T-S) relation-  
243 ships [*Thacker*, 2008]. Below 800 m, the temperature and salinity profiles are extended  
244 down to the bottom of the ocean with their climatological values [*Baringer and Garzoli*,  
245 2007; *Dong et al.*, 2009]. The barotropic or external mode is generally estimated by adopt-

246 ing a level of no motion at the depth where the potential density anomaly referenced to  
247 2000 dbar assumes the value of  $37.09 \text{ Kg m}^{-3}$  ( $\sigma_2 = 37.09$ ) [*Ganachaud and Wunsch,*  
248 *2003; Baringer and Garzoli, 2007*]. The  $\sigma_2 = 37.09$  depth is approximately located at  
249 3700 m depth and between two water masses, the North Atlantic Deep Water (NADW)  
250 flowing southward between 1500 and 3700 m, and the underlying Antarctic Bottom Water  
251 (AABW) flowing northward [*Ganachaud and Wunsch, 2003*]. The Ekman component of  
252 the flow is calculated from available zonal wind stress products at the XBT deployment  
253 locations.

254 In order to simulate the XBT observations in the model, we make the same assumptions  
255 as used in the observational studies: i) the model temperature data are used above 800  
256 m, ii) a quadratic least squares fit between the annual mean temperature and salinity  
257 obtained from the model is specified for each depth, calculated using 1 degree boxes along  
258  $34^\circ\text{S}$ , iii) the monthly climatology of temperature and salinity at a 1 degree longitudinal  
259 resolution is padded below 800 m to extend the pseudo-observations to the bottom of  
260 the ocean, and iv) a reference level for the geostrophic velocity calculation is chosen.  
261 Constructing the T-S relationships from the model instead of using, for example, the  
262 World Ocean Atlas (WOA) climatology is necessary, since the model's own internal biases  
263 relative to the observations could potentially bring spurious T-S discontinuities. WOA  
264 climatology is subject to biases in regional coverage, such as below 2000 m (the parking  
265 depth of Argo floats), along coastal areas, and historically in the South Atlantic. Here,  
266 we do not account for imperfect sampling although its effects can be sizeable in producing  
267 additional seasonal biases.

268 The RMS error between the model salinity and the salinity estimated from the lookup  
269 table is shown in Figure 6. In the top 200 m, salinity errors are on the order of 0.1 psu.  
270 Higher differences ( $\sim 0.4$  psu) are found in the western side of the basin in the upper 100  
271 m, where there is a fresh water inflow from river runoff. Below 200 m the RMS difference  
272 is generally lower than 0.1 psu, with higher values located around 500 m and decreasing  
273 to near zero below 1000 m. These error values are on the same order of magnitude of the  
274 RMS of the salinity annual cycle and, therefore, are highly driven by the seasonal variation  
275 of T-S relationships, which is not captured by the annual mean T-S relationships.

276 It is also important to mention that XBT measurements do not contain pressure infor-  
277 mation, and depth estimates follow a fall rate equation (FRE) that is a quadratic function  
278 of the time of descent of the probe. The FRE is subject to parametric uncertainties, which  
279 translate into depth biases with typical values of the order 2% of depth [*Goes et al.*, 2013a].  
280 The AMOC and MHT estimated errors associated with a typical FRE bias in the upper  
281 800 m are  $-0.06 \pm 0.07$  Sv and  $-0.01 \pm 0.01$  PW, respectively, which are small compared  
282 to the other observational assumptions considered here.

### 5.3. AMOC and MHT uncertainties due to the XBT transect observational sampling

283 In this section we investigate the meridional transport uncertainties associated with the  
284 observational sampling. We will explore two main sources of uncertainty, i) the tempo-  
285 ral resolution and ii) the horizontal resolution. We apply each of the two assumptions  
286 individually in order to quantify their uncertainties, which will allow recommending im-  
287 provements in the AX18 transect design and implementation.

#### 5.3.1. Temporal resolution



289 The AX18 transect was originally implemented to be carried out four times a year,  
290 and estimates of the geostrophic AMOC transport can only be performed at the time  
291 of each AX18 transect realization. The rate of time sampling as well as the year-to-  
292 year variability of number of transects may alias the estimates of the annual cycle of the  
293 AMOC and meridional heat transport [*Bryden et al.*, 2005]. We simulate in the model  
294 uncertainties associated with the transect temporal sampling by randomly selecting points  
295 in the timeseries of the geostrophic AMOC and MHT, and use the RMS difference of  
296 monthly means of these two quantities as a measure of the uncertainty associated with the  
297 temporal sampling. We vary two parameters associated with the temporal sampling of the  
298 AX18 transect: The number of realizations per year, from 1 to 20 times per year, and the  
299 number of years of data collection, from 1 to 15 years. The random sampling is calculated  
300 in three steps. First the original timeseries of the AMOC and MHT are extended by  
301 padding up to 100 years. Some small stochastic noise is added to the extended timeseries.  
302 Seasonality is maintained in this timeseries by choosing accordingly the beginning of  
303 each padded timeseries. Second, a stretch of the 100-year timeseries is chosen with its  
304 length defined by the uncertain parameter number of years sampled. Third, according  
305 the number of samples per year, random samples are taken from the stretch of the time  
306 series. In this step the samples are evenly distributed around the year, for example, with  
307 a two sample per year parameter setting, one sample is taken every semester. These  
308 steps are reproduced 400 times, which is a number sufficiently high to allow all months  
309 to be sampled and the average of all realizations to have the same monthly means as  
310 the original model geostrophic AMOC and MHT. Furthermore, the mean monthly RMS  
311 difference of the 400 realizations will define a measure of the uncertainty associated with

312 the time sampling. Contour plots showing the sampling error variability of the AMOC  
313 and MHT with respect to the number of years measured and the number of samples per  
314 year is shown in Figure 7. The time sampling error of the AMOC and MHT show similar  
315 behavior, i.e., errors decrease exponentially as more samples are collected during the year  
316 or when a higher number of years is sampled. The RMS errors are as low as 0.5 Sv  
317 and 0.05 PW when carrying out up to 12 transect realizations per year for 15 years. On  
318 the other hand, when transects are carried out twice a year for two years, the errors are  
319 above 2.4 Sv and 0.25 PW, respectively. The current number of realizations of the AX18  
320 transect along the nominal of 34°S is 18 (Figure 2), which are done approximately on a  
321 quarterly basis. This is equivalent to a total sampling period of five years in our considered  
322 parameter space. Therefore, according to our model estimates, the associated RMS errors  
323 of the AMOC and MHT are 2.3 Sv and 0.24 PW, respectively (stars in Figure 7), close  
324 to the most uncertain values in the studies parameter space. Although 12 realizations  
325 per year is difficult to achieve operationally, current discussions for increasing the number  
326 of transect realizations to five or six per year are underway. This would lower the RMS  
327 errors to  $< 2$  Sv for the AMOC and  $< 0.2$  PW for the MHT, which may allow a greater  
328 improvement over the years.

329 One additional temporal sampling error arises from the non-synopticity of the XBT  
330 transect measurements. An AX18 realization takes approximately 10 days to complete  
331 the trajectory from South America to Cape Town, which may alias the transport estimates  
332 across this transect. We quantify here the errors due to non-synopticity by simulating the  
333 same observational assumptions within the model environment. In this experiment, we  
334 simulate one AX18 XBT realization for each model day by using 10 bins of meridional

335 velocity values from east to west that correspond to 10 consecutive days of model velocity.  
336 The AMOC and MHT are estimated every 7 days from these simulations, using as the  
337 time tag the first day of each non-synoptic field. These estimates are compared against  
338 the ones from the synoptic model outputs. The errors associated with the non-synopticity  
339 of the data for the whole period of the simulation are  $0.22 \pm 4.2$  Sv for the AMOC and  
340  $0.02 \pm 0.24$  PW for MHT. The RMS values due to non-synopticity are on the same order  
341 as the RMS errors produced by the quarterly sampling. However, since this calculation  
342 is performed over model daily values instead of 7-day averages, these RMS values are  
343 actually an overestimation in comparison to the other experiments.

### 344 **5.3.2. Horizontal sampling**

345 The AX18 XBT transect crosses three regions of different dynamic regimes (Figure  
346 1): i) the western (Confluence region), interior (gyre), and eastern (Agulhas leakage).  
347 Previous studies suggest that it is critical to account for the variability in all three regions  
348 in order to monitor and quantify changes in the AMOC and MHT [*Dong et al.*, 2009]. The  
349 current XBT spatial sampling strategy accounts for the different regional characteristics:  
350 at a lower density ( $\sim 50$  km) in the interior region, and at higher density ( $\sim 25$  km) closer  
351 to the boundaries, i.e., east of the Walvis Ridge ( $\sim 1^\circ$ W) and west of  $40^\circ$ W, outside the  
352 continental slope region in South America. This sampling strategy is a heuristic approach  
353 to add more spatial resolution to the high energy boundary regions (Figure 1). Here we  
354 quantify the sensitivity of the meridional transport changes to the horizontal sampling  
355 in these three regions. To accomplish this, we generate an ensemble with 30 members  
356 by degrading the longitudinal resolution in each of the three regions at a time, from the  
357 original 0.08 degree ( $\sim 7.3$  km) model grid up to 5 degrees ( $\sim 460$  km) at variable steps,

358 giving more emphasis to the high resolution sampling. We use the RMS error, bias, and  
359 correlation as metrics to compare the reconstructions to the original AMOC and MHT  
360 strength.

361 Our results show that the AMOC strength and MHT are less sensitive to changes in the  
362 spatial resolution in the interior than at the boundary regions (Figure 8). For the AMOC,  
363 degrading the resolution in the interior to a  $5^\circ$  degree longitude sampling produces a small  
364 negative bias and RMS error of  $-0.6 \pm 1.5$  Sv, and a correlation of  $\sim 0.9$ . In the boundary  
365 regions, the AMOC and MHT are more sensitive to changes in spatial sampling. The  
366 bias and RMS error for a 25 km ( $\sim 0.3^\circ$ ) spacing is of  $2.8 \pm 3.2$  Sv in the western and  
367  $0.23 \pm 1.2$  Sv in the eastern boundary. The correlation is about 0.9 at 25 km spacing in  
368 the boundaries, and decreases to 0.6 when longitudinal sampling is larger than  $\sim 90$  km  
369 ( $1^\circ$ ). The larger decrease of correlation in the boundaries is partly due to subsampling  
370 of strong currents and high mesoscale activity, and also because the shelf transport may  
371 not be observed at lower sampling rates. The potentially unresolved volume transports  
372 in the continental shelves (above 200 m deep) are  $-0.61 \pm 0.77$  Sv in the west and  $0.15 \pm$   
373  $0.44$  Sv in the east of the basin. Both transports on the shelf contribute only a negligible  
374 temperature transport ( $\sim 10^{-8}$  PW), which agrees with the estimates of *Baringer and*  
375 *Garzoli* [2007]. Therefore, a high AX18 horizontal sampling is indeed needed in the eastern  
376 and western boundaries, especially in the western side of the basin where biases are larger  
377 at the current sampling in comparison to the other regions.

378 Interestingly, biases in the AMOC strength and MHT have opposite signs and similar  
379 magnitudes when comparing the western and eastern boundaries for any given zonal

380 sampling resolution (Figure 8c, f). Therefore, biases in the eastern and western regions  
381 may cancel each other to some extent.

## 5.4. AMOC and MHT uncertainties due to computational methodology

382 In the previous section we analyzed the sensitivity of the AMOC and MHT to strategies  
383 for different temporal and spatial sampling of the AX18 XBT transect. In this section,  
384 we investigate how methodological assumptions affect the AMOC and MHT estimated  
385 at 34°S. First, we will explore the impact of salinity and deep temperature inferences.  
386 Additionally, we optimize the choice of the reference level, and propose a method to  
387 estimate the barotropic velocities across the transect.

### 5.4.1. Salinity and deep temperature inferences

389 To study the impact of salinity and deep temperature inferences on the AMOC and  
390 MHT, we perform step changes in the model observational strategy. We compute  $\Psi_y$   
391 and MHT using: i) the constructed annual T-S lookup table (Section 5.1) to estimate  
392 salinity profiles in the upper 800 m, ii) padding the model T-S monthly climatology in  
393 the deep ocean ( $> 800$  m deep), and iii) using both the lookup table in the upper ocean  
394 and padding in the deeper ocean.

395 We compare the changes in the geostrophic components of AMOC strength and MHT  
396 using these approximations against those calculated using the full model output. The main  
397 variability of the AMOC and MHT follow closely the ones from the approximated fields. In  
398 a closer analysis of the residuals with respect to the estimates from the full model outputs  
399 (Figure 9), the AMOC residuals show that the T-S lookup approximation drives most  
400 of the residual changes ( $-0.33 \pm 2.6$  Sv). Residuals from the T-S lookup approximation  
401 are subject to strong seasonality as observed during austral winter, when biases can reach

402 almost -2 Sv. This seasonal bias is due to the fact that the T-S relationships are taken from  
403 an annual mean. Deep ocean padding biases show only a small seasonality, and AMOC  
404 mean biases are small, with magnitude of  $0.06 \pm 2.3$  Sv. For the MHT, performing either  
405 padding or TS lookup approximations produce residual changes of  $-0.03 \pm 0.14$  PW and  
406  $0.02 \pm 0.16$  PW, respectively. The RMS error calculated here is close to the value of  $\pm$   
407  $0.15$  PW estimated using the cumulative transport of one A10 section in *Baringer and*  
408 *Garzoli* [2007]. The results of our analysis using a six-year timeseries show that although  
409 the errors produced by salinity and deep temperature approximations are similar in value,  
410 the seasonal amplitude of the MHT and AMOC residuals using the TS lookup table is the  
411 largest (right panels in Figures 9a and 9b). Although these are conservative estimates,  
412 given that the model climatology represents well the variability below the surface, the  
413 errors caused by deep T-S padding are small in comparison to the other sources. Thus  
414 deployment of a whole water column CTD is not essential for a strong reduction of errors  
415 in the AX18 XBT transect.

#### 416 **5.4.2. Reference level for absolute geostrophic velocities**

417 The barotropic mode accounts for most of the bias of the overturning circulation con-  
418 tribution [*Baehr et al.*, 2004]. As indicated from the model output (Figure 10), variations  
419 in bottom topography are the main driver of strong bottom velocities, which increases the  
420 barotropic contribution and its potential biases as well. Zonal sections, where boundaries  
421 are steeper and more similar to a vertical wall, can reduce the effect of the barotropic  
422 contribution [*Rayner et al.*, 2011]. At  $34^{\circ}\text{S}$ , where there are strong bottom velocities,  
423 large biases in the barotropic component could be introduced by assuming an inaccurate  
424 reference velocity. Here we perform four experiments to estimate the sensitivity of the

425 barotropic AMOC ( $\Psi_{bar}$ ) to the velocity of the reference level. Similar to observational  
426 studies, we use in all experiments the reference depth at the  $\sigma_2 = 37.09$ . Since the velocity  
427 at the depth of  $\sigma_2 = 37.09$  is below 3000 m, it is not well constrained by observations.  
428 Therefore we perform the following experiments: a) with zero reference velocity, b) with  
429 climatological reference velocity at the western boundary, c) with climatological reference  
430 velocity at the eastern boundary, and d) with climatological velocity at both western  
431 and eastern boundaries. Figure 11 shows the evolution and the time mean barotropic  
432 streamfunction (left and right panels, respectively), for the experiments (a-d).

433 The minimum of barotropic streamfunction, which characterizes its strength, is located  
434 between 2 and 3 km deep. Using model velocities, the mean  $\Psi_{bar}$  strength is estimated  
435 as -16.3 Sv. When zero reference velocity is assumed, a much weaker  $\Psi_{bar}$  strength value  
436 is estimated ( $\Psi_{bar} = -9.0$  Sv; Figure 11a), or a mean bias of  $7.2 \pm 8.45$  Sv. Because the  
437 barotropic streamfunction is the main balance of the vertical shear component in the model  
438 (Figure 3), a weaker  $\Psi_{bar}$  acts to increase the MHT by  $0.16 \pm 0.22$ . Adding a climatological  
439 reference velocity in the boundaries reduces the uncertainties in the barotropic mode. The  
440 derived  $\Psi_{bar}$  strength estimates using climatological reference velocities in the boundaries  
441 produce positive biases of  $5.5 \pm 7.1$  Sv ( $0.06 \pm 0.16$  PW) in the western boundary and  
442  $3.5 \pm 5.6$  Sv ( $0.08 \pm 0.21$  PW) in the eastern side of the basin (Figures 11b and 11c,  
443 respectively). Therefore, the eastern boundary velocity information reduces uncertainties  
444 more than in the western boundary. When both eastern and western reference velocities  
445 are added (Figure 11d), the mean  $\Psi_{bar} = -14.4$  Sv, and the  $\Psi_{bar}$  strength is correctly  
446 measured at value of  $1.9 \pm 4.7$  Sv ( $0.02 \pm 0.13$  PW). Further adding reference velocity  
447 information in the interior does not improve these uncertainty values.

448 Therefore, we show here that the misrepresentation of the reference velocities in the  
449 geostrophic calculation yields the highest contribution to the uncertainties in the AMOC  
450 and MHT calculations. Knowledge of the reference level velocities at both the western and  
451 eastern boundaries is necessary for considerably reducing the mean bias in the barotropic  
452 mode. This can be achieved by using climatological values in the boundaries, and this  
453 information may be acquired from available Argo float climatologies [e.g., *Goes et al.*,  
454 2013b], for example. However, climatological reference velocities still produce relatively  
455 large biases ( $1.9 \pm 5.2$  Sv and  $0.02 \pm 0.13$  PW) due to the high variability of the barotropic  
456 mode in the region. To tackle the high frequency variability of the barotropic mode,  
457 additional available observations can be used. This question is addressed in the next  
458 section.

### 459 **5.4.3. Alternative barotropic velocity estimation using altimetry and hydrog-** 460 **raphy**

461 In order to optimize the information necessary to monitor the AMOC at  $34^\circ\text{S}$ , several  
462 additional observations could be used to complement the AX18 XBT transect measure-  
463 ments. Some complimentary observations are already in place, such as the satellite wind  
464 stress measurements used to estimate the Ekman transport.

465 A topic of current research in the AMOC decomposition is the estimation of the  
466 barotropic mode. Using a reference level near the bottom of the ocean cannot capture  
467 interannual or longer variability due to the presence of deep flows, since in this work cli-  
468 matology is assumed below 800 m. Bottom pressure ( $P_{bot}$ ) recorders are a useful platform  
469 to compute the time varying reference level for the meridional geostrophic velocity, and,  
470 therefore, estimate the non-steric component of the sea level height (SLH). Such a plat-



471 form requires further investment in an array across the basin, and efforts are underway  
472 [*Perez et al.*, 2011; *Meinen et al.*, 2012]. Some recent studies use a blend of altimetry  
473 and Argo parking velocity as the reference level or level of known motion to infer abso-  
474 lute geostrophic velocities [*Willis and Fu*, 2008; *Mielke et al.*, 2013; *Goes et al.*, 2013b].  
475 However, because a large number of Argo floats is necessary to produce a reliable esti-  
476 mate, seasonal averages are generally used in an Argo-based reference level. We showed  
477 in the previous section that a climatological assumption of the reference velocity in the  
478 eastern and western boundaries can reduce the AMOC mean bias considerably. Here  
479 we test another method for measuring the barotropic flow by using SLH derived from  
480 satellite altimetry in conjunction with hydrographic data. Altimetry captures both steric  
481 and non-steric components, whose contributions are variable among different regions of  
482 the ocean [*Guinehut et al.*, 2006]. The non-steric contribution generally increases toward  
483 higher latitudes due to weaker stratification and stronger Coriolis force. In some regions  
484 the non-steric contributions, such as the barotropic component, can account for more than  
485 50% of the total sea level variability [*Shriver and Hurlburt*, 2000].

486 Using a hydrostatic relation, the non-steric sea level can be accurately related to bot-  
487 tom and atmospheric ( $P_{atm}$ ) pressure [*Park and Watts*, 2005] as  $SLH = (P_{bot} - \rho_0 g H -$   
488  $P_{atm}) / \rho_0 g$ . In order to estimate the non-steric component of the sea level, we filter the  
489 steric contribution by calculating the residual between SLH and the dynamic height (DH)  
490 referenced at a certain level ( $SLH - DH$ ). The barotropic velocities are calculated using  
491 geostrophy on this residual field, and the maximum barotropic streamfunction calculated  
492 from these velocities is then compared to the model barotropic streamfunction.

493 We consider DH referenced at a certain depth, and estimate the optimal reference depth  
494 by varying the reference of DH from 300 m down to 3500 m deep (Figure 12). According to  
495 our results, the structure of the variability of the barotropic velocities can be well captured  
496 by the non-steric sea level. The strength of the barotropic AMOC show correlations above  
497 0.6 irrespective of the reference level used in the DH estimation. High correlations ( $> 0.9$ )  
498 are found for a DH reference level between 500 m and 1000 m. A minimum RMS region  
499 ( $< 5$  Sv) overlaps with the maximum correlation region, and it is found for a reference  
500 level between 700-1100 m (Figure 12a). The minimum RMS error of  $\sim 3$  Sv is achieved  
501 when DH is referenced at 1000 m. Finally, we quantify how much information is gained by  
502 using altimetry data instead of using the  $\sigma_2 = 37.09$  as a level of no motion for barotropic  
503 velocity. The barotropic streamfunction strength using the  $\sigma_2 = 37.09$  reference level  
504 shows RMS error and correlation of 9 Sv and 0.78, respectively. Using altimetry and DH  
505 referenced at 800 m, the maximum depth of an XBT profile, promotes a reduction of 4  
506 Sv in RMS and an increase of 0.15 in correlation towards this density reference level.  
507 Although we did not include measurement errors in these estimates, this result is a proof  
508 of concept that altimetry and XBT data are complementary platforms for the inference  
509 of the long term variability of the AMOC.

## 6. Conclusions

510 In this study we use a high resolution model assimilation product to assess the observa-  
511 tional and computational uncertainties associated with estimating meridional transports  
512 using the data from the AX18 XBT transect along  $34^\circ\text{S}$ . We analyzed the AMOC and  
513 MHT in terms of their vertical shear, barotropic, and Ekman components. These terms  
514 are here used to reconstruct the AMOC and MHT. We show that this method is well

515 suited for this type of work. In comparison to the AMOC calculated from the model  
516 velocities, the reconstructed AMOC streamfunction is able to represent the main model  
517 features, although the reconstruction cannot capture the high frequency reversals of the  
518 model AMOC and MHT during austral winter/spring. A key finding obtained here is  
519 that XBTs produce acceptable estimates of the AMOC and MHT variability, where the  
520 uncertainties obtained by the multiple sources of error are smaller than the signal of the  
521 time series variability. Therefore, the AX18 transect is a valuable and longstanding piece  
522 of a multiple platform monitoring system for the region, and efforts should be made to  
523 maintain and improve it. The results obtained here are summarized in Table 1, and the  
524 results of *Baringer and Garzoli* [2007] for MHT is added for comparison. As follows, we  
525 make recommendations for optimization of sampling and computational methodologies to  
526 improve estimates of the AMOC and meridional MHT:

527 • The effect of T-S padding from monthly climatology below 800 m on the AMOC  
528 ( $0.06 \pm 2.6$  Sv) and MHT ( $-0.03 \pm 0.14$ ) estimates is small in comparison to the other  
529 error sources. The effect of using salinity from the T-S lookup table in the upper 800 m is  
530 also small in comparison to the other components, and is about the same order as the deep  
531 ocean padding. However, due to seasonal biases, monthly biases can reach 2 Sv. Salinity  
532 from other measurements, such as Argo or monthly climatology T-S relationships, would  
533 avoid these seasonal biases.

534 • Current quarterly sampling causes an average RMS error of  $\pm 2.3$  Sv and  $\pm 0.24$  PW  
535 in the climatological AMOC and MHT estimates, respectively. The optimal strategy to  
536 reduce this sampling error would be to carry out 12 transects per year, i.e. one per month,

537 which is not feasible due to operational constraints. More realistically, it is desirable to  
538 conduct continuous realizations at current quarterly sampling for at least 15 years.

539 • Spatial subsampling in the interior produces small errors in the AMOC and MHT  
540 estimates compared to the errors produced at the boundaries. The current AX18 zonal  
541 sampling uses 25 km on the boundaries and 50 km in the interior of the basin. This  
542 current spatial sampling seems to be adequate to capture most of the variability of the  
543 meridional transports, although the western boundary resolution still shows large AMOC  
544 and MHT biases at the present sampling ( $2.8 \pm 3.2$  Sv and  $0.13 \pm 0.14$  PW). An increase  
545 in the western boundary sampling to 20 km would improve current AMOC results, and  
546 it would capture better the variability of the shelf transport.

547 • As described in previous studies [e.g., *Kanzow et al.*, 2007, for  $26.5^\circ\text{N}$ ], the barotropic  
548 mode is likely to be the most significant source of errors in the AMOC and MHT calcu-  
549 lations due to the extensive continental shelf along  $34^\circ\text{S}$ . Errors are on the order of  $7.2 \pm$   
550  $8.45$  Sv for the AMOC and  $0.16 \pm 0.22$  PW for MHT if a level of no motion is used in  
551  $\sigma_2 = 37.09$   $\text{kgm}^{-3}$ . Using at least climatological values as the reference velocities in both  
552 boundaries is necessary to reduce the AMOC and MHT biases to  $\sim 1.9 \pm 5.2$  Sv and  $0.02$   
553  $\pm 0.13$  PW, respectively.

554 • The use of satellite altimetry observations in conjunction with hydrographic data  
555 is a good alternative for barotropic term estimation. We show that barotropic volume  
556 transport estimates using the non-steric component of altimetry can improve the RMS  
557 error by  $\sim 3$  Sv in comparison to the commonly used level of no motion at  $\sigma_2 = 37.09$   
558  $\text{kgm}^{-3}$ .

559 Finally, this study assesses only one the part of the several platforms that are in place to  
560 monitor the variability of the AMOC and MHT in the South Atlantic, XBT and altimetry  
561 data. The utility of the other operational platforms, such as moorings and Argo data,  
562 has been demonstrated in various other studies [*Dong et al.*, 2011b; *Perez et al.*, 2011].  
563 An analysis that includes a blend of several platforms is still necessary to evaluate the  
564 optimal observational system for the region.

565 **Acknowledgments.** The authors want to thank Joe Metzger for providing the  
566 GLBa0.08/74.2 simulation output, and the ship companies Evergeen Lines, CMA CGM  
567 Lines, Hamburg Sud and Monte Azul for carrying out the AX18 cruises as part of the  
568 Ships of Opportunity project. This research was accomplished under the auspices of  
569 the Cooperative Institute for Marine and Atmospheric Studies (CIMAS), a cooperative  
570 institute of the University of Miami and the National Oceanic and Atmospheric Admin-  
571 istration, cooperative agreement #NA17RJ1226, and was partly funded by the NOAA  
572 Climate Program Office.

## References

- 573 Baehr, J., J. Hirschi, J.-O. Beismann, and J. Marotzke (2004), Monitoring the meridional  
574 overturning circulation in the North Atlantic: A model-based array design study, *J.*  
575 *Mar. Res.*, *62*(3), 283–312, doi:10.1357/0022240041446191.
- 576 Baehr, J., D. McInerney, K. Keller, and J. Marotzke (2008), Optimization of an observing  
577 system design for the North Atlantic meridional overturning circulation, *J. Atmosph.*  
578 *Ocean. Tech.*, *25*(4), 625–634, doi:10.1175/2007JTECHO535.1.

579 Baringer, M., and S. Garzoli (2007), Meridional heat transport determined with expend-  
580 able bathythermographs, Part I: Error estimates from model and hydrographic data,  
581 *Deep-Sea Res. I*, *54*(8), 1390–1401, doi:10.1016/j.dsr.2007.03.011.

582 Beal, L. M., W. P. M. D. Ruijter, A. Biastoch, R. Zahn, and S. 136 (2011), On the role  
583 of the Agulhas system in ocean circulation and climate, *Nature*, *472*(7344), 429–436,  
584 doi:10.1038/nature09983.

585 Biastoch, A., C. W. Böning, F. U. Schwarzkopf, and J. R. E. Lutjeharms (2009), Increase  
586 in Agulhas leakage due to poleward shift in the southern hemisphere westerlies, *Nature*,  
587 *462*, 495–498, doi:10.1038/nature08519.

588 Bryden, H. L., H. R. Longworth, and S. A. Cunningham (2005), Slowing of the  
589 Atlantic meridional overturning circulation at 25°N, *Nature*, *438*, 655–657, doi:  
590 10.1038/nature04385.

591 Chassignet, E., H. Hurlburt, E. Metzger, O. Smedstad, J. Cummings, G. Halliwell,  
592 R. Bleck, R. Baraille, A. Wallcraft, C. Lozano, H. Tolman, A. Srinivasan, S. Han-  
593 kin, P. Cornillon, R. Weisberg, A. Barth, R. He, F. Werner, and J. Wilkin (2009), U.S.  
594 GODAE: Global ocean prediction with the hybrid coordinate ocean model (HYCOM),  
595 *Oceanography*, *22*(2), 64–75, doi:10.5670/oceanog.2009.39.

596 Cummings, J. A. (2005), Operational multivariate ocean data assimilation, *Quart. J.*  
597 *Royal Met. Soc., Part C*, *131*(613), 3583–3604, doi:10.1256/qj.05.105.

598 Dong, B.-W., and R. T. Sutton (2007), Enhancement of El Nino-Southern Oscillation  
599 ENSO variability by a weakened Atlantic thermohaline circulation in a coupled GCM,  
600 *J. Clim.*, *20*, 4920–4939, doi:10.1016/j.dsr2.2010.10.069.

601 Dong, S., S. L. Garzoli, M. O. Baringer, C. S. Meinen, and G. J. Goni (2009), Interannual  
602 variations in the Atlantic meridional overturning circulation and its relationship with the  
603 net northward heat transport in the South Atlantic, *Geophys. Res. Lett.*, *36*, L20,606,  
604 doi:10.1029/2009GL039356.

605 Dong, S., S. Garzoli, and M. Baringer (2011a), The role of interocean exchanges on decadal  
606 variations of the meridional heat transport in the South Atlantic, *J. Phys. Oceanogr.*,  
607 *41*, 1498–1511, doi:10.1175/2011JPO4549.1.

608 Dong, S., M. Baringer, G. Goni, and S. Garzoli (2011b), Importance of the assimilation  
609 of Argo float measurements on the meridional overturning circulation in the South  
610 Atlantic, *Geophys. Res. Lett.*, *38*, L18,603, doi:10.1029/2011GL048982.

611 Donners, J., and S. S. Drijfhout (2004), The lagrangian view of South Atlantic intero-  
612 cean exchange in a global ocean model compared with inverse model results, *J. Phys.*  
613 *Oceanogr.*, *34*, 1019–1035, doi:10.1175/1520-0485(2004)034<1019:TLVOSA>2.0.CO;2.

614 Ducet, N., P.-Y. L. Traon, and G. Reverdin (2000), Global high-resolution mapping of  
615 ocean circulation from Topex/Poseidon and ERS-1 and -2, *J. Geophys. Res.*, *105 (C8)*,  
616 19,477–19,498, doi:10.1029/2000JC900063.

617 Enfield, D. B., A. M. Mestas-Nuez, and P. J. Trimble (2001), The Atlantic Multidecadal  
618 Oscillation and its relation to rainfall and river flows in the continental U.S., *Geophysical*  
619 *Research Letters*, *28(10)*, 2077–2080, doi:10.1029/2000GL012745.

620 Fox, D., W. J. Teague, C. N. Barron, M. R. Carnes, and C. M. Lee (2002), The modular  
621 ocean data assimilation system (MODAS), *J. Atmos. Ocean. Technol.*, *19*, 240–252,  
622 doi:10.1175/1520-0426(2002)019<0240:TMODAS>2.0.CO;2.

623 Ganachaud, A., and C. Wunsch (2003), Large scale ocean heat and freshwater trans-  
624 ports during the World Ocean Circulation Experiment, *J. Climate*, *16*, 696–705, doi:  
625 10.1175/1520-0442(2003)016<0696:LSOHAF>2.0.CO;2.

626 Garzoli, S. (1993), Geostrophic velocities and transport variability in the Brazil/Malvinas  
627 confluence, *Deep-Sea Res.*, *40*, 1379–1403, doi:10.1016/0967-0637(93)90118-M.

628 Garzoli, S., and M. Baringer (2007), Meridional heat transport determined with expend-  
629 able bathythermographs. Part II: South Atlantic transport, *Deep-Sea Res. I*, *54*, 1402–  
630 1420, doi:10.1016/j.dsr.2007.04.013.

631 Garzoli, S., M. Baringer, S. Dong, R. Perez, and Q. Yao (2013), South Atlantic meridional  
632 fluxes, *Deep-Sea Res. I*, *71*, 21–32, doi:10.1016/j.dsr.2012.09.003.

633 Garzoli, S. L., and R. Matano (2011), The South Atlantic and the Atlantic merid-  
634 ional overturning circulation, *Deep-Sea Res. Part II*, *58*(17–18), 1837–1847, doi:  
635 10.1016/j.dsr2.2010.10.063.

636 Goes, M., N. M. Urban, R. Tonkonojekov, M. Haran, A. Schmittner, and K. Keller  
637 (2010), What is the skill of ocean tracers in reducing uncertainties about ocean diapycnal  
638 mixing and projections of the atlantic meridional overturning circulation?, *J. Geophys.*  
639 *Res.*, *115*, C12,006, doi:10.1029/2010JC006407.

640 Goes, M., G. Goni, and K. Keller (2013a), Reducing biases in XBT measurements by  
641 including discrete information from pressure switches, *J. Atmos. Oceanic Technol.*, *30*,  
642 810–824, doi:10.1175/JTECH-D-12-00126.1.

643 Goes, M., G. Goni, V. Hormann, and R. Perez (2013b), Variability of the Atlantic off-  
644 equatorial eastward currents during 1993-2010 using a synthetic method, *J. Geophys.*  
645 *Res.-Oceans*, *118*(6), 3026 – 3045, doi:10.1002/jgrc.20186.



646 Goni, G., and I. Wainer (2001), Investigation of the Brazil Current front variability from  
647 altimeter data, *J. Geophys. Res.*, *106*, 31,117–31,128, doi:10.1029/2000JC000396.

648 Goni, G., S. Garzoli, A. Roubicek, D. Olson, and O. Brown (1997), Agulhas ring dynamics  
649 from TOPEX/POSEIDON satellite altimeter data, *J. Mar. Res.*, *55*(5), 861–883, doi:  
650 10.1357/0022240973224175.

651 Goni, G., F. Bringas, and P. D. Nezio (2011), Observed low frequency variability of the  
652 Brazil Current front, *J. Geophys. Res.*, *116*, C10,037, doi:10.1029/2011JC007198.

653 Gordon, A. (1986), Interocean exchange of thermocline water, *J. Geophys. Res.*, *91*, 5037–  
654 5046, doi:10.1029/JC091iC04p05037.

655 Griffies, S. M., M. J. Harrison, R. C. Pacanowski, and A. Rosati (2004), A technical guide  
656 to MOM4, GFDL Ocean Group, *Tech. Rep. 5*, NOAA/GFDL, Princeton, NJ.

657 Guinehut, S., P.-Y. L. Traon, and G. Larnicol (2006), What can we learn from  
658 global altimetry/hydrography comparisons?, *Geophys. Res. Lett.*, *33*, L10,604, doi:  
659 10.1029/2005GL0255551.

660 Hall, M. M., and H. L. Bryden (1982), Direct estimates and mechanisms of ocean heat  
661 transport, *Deep-Sea Res.*, *29*(3), 339–359, doi:10.1016/0198-0149(82)90099-1.

662 Hatun, H., A.-B. Sandø, H. Drange, B. Hansen, and H. Valdimarsson (2005), Influence  
663 of the atlantic subpolar gyre on the thermohaline circulation, *Science*, *309*, 1841–1844,  
664 doi:10.1126/science.1114777.

665 Hawkings, E., R. S. Smith, L. C. Allison, J. M. Gregory, T. J. Woollings, H. Pohlmann,  
666 and B. de Cuevas (2011), Bistability of the Atlantic overturning circulation in a global  
667 climate model and links to ocean freshwater transport, *Geophys Res Lett.*, *38*, L10,605,  
668 doi:10.1029/2011GL047208.

669 Hirschi, J., J. Baehr, J. Marotzke, J. Stark, S. Cunningham, and J.-O. Beismann (2003),  
670 A monitoring design for the Atlantic meridional overturning circulation, *Geophys. Res.*  
671 *Lett.*, *30*, 1413, doi:10.1029/2002GL016776.

672 Hu, A., G. A. Meehl, W. Han, and J. Yin (2011), Effect of the potential melting of the  
673 Greenland ice sheet on the meridional overturning circulation and global climate in the  
674 future, *Deep-Sea Res. II*, *58*, 1914–1926, doi:10.1029/2000GL012745.

675 Jayne, S. R., and J. Marotzke (2001), The dynamics of ocean heat transport variability,  
676 *Rev. Geophys.*, *39*, 385–411, doi:10.1029/2000RG000084.

677 Kanzow, T., S. A. Cunningham, D. Rayner, J. J.-M. Hirschi, W. E. Johns, M. O. Baringer,  
678 H. L. Bryden, L. M. Beal, C. S. Meinen, and J. Marotzke (2007), Observed flow compen-  
679 sation associated with the MOC at 26.5 degrees N in the Atlantic, *Science*, *317*(5840),  
680 938–941, doi:10.1126/science.1141293.

681 Lee, T., and J. Marotzke (1998), Seasonal cycles of meridional overturning and heat  
682 transport of the Indian Ocean, *J. Phys. Oceanogr.*, *28*, 923–943, doi:10.1175/1520-  
683 0485(1998)028<0923:SCOMOA>2.0.CO;2.

684 Lentini, C., G. Goni, and D. Olson (2006), Investigation of Brazil Current rings in the  
685 confluence region, *J. Geophys. Res.*, *111*(C06013), doi:10.1029/2005JC002988.

686 Levermann, A., A. Griesel, M. Hofmann, M. Montoya, and S. Rahmstorf (2005), Dynamic  
687 sea level changes following changes in the thermohaline circulation, *Climate Dyn.*, *24*,  
688 347–354, doi:10.1007/s00382-004-0505-y.

689 Locarnini, R. A., A. V. Mishonov, J. I. Antonov, T. P. Boyer, and H. E. Garcia (2006),  
690 World Ocean Atlas 2005, *Tech. Rep. V. 1: Temperature*, NOAA Atlas NESDIS 61, U.S.  
691 Government Printing Office, Washington, D.C.

692 Lohmann, K., H. Drange, and M. Bentsen (2009), A possible mechanism for the strong  
693 weakening of the north atlantic subpolar gyre in the mid-1990s, *Geophys. Res. Lett.*,  
694 *36*, L15,602, doi:1029/2009GL039166.

695 Marshall, J., and F. Schott (1999), Open-ocean convection: Observations, theory and  
696 models, *Rev. Geophys.*, *37*, 1–64, doi:10.1029/98RG02739.

697 Meinen, C. S., A. R. Piola, R. C. Perez, and S. L. Garzoli (2012), Deep Western Boundary  
698 Current transport variability in the South Atlantic: preliminary results from a pilot  
699 array at 34.5° S, *Ocean Sci. Discuss.*, *9*, 977–1008, doi:10.5194/osd-9-977-2012.

700 Mielke, C., E. Frajka-Williams, and J. Baehr (2013), Observed and simulated variabil-  
701 ity of the AMOC at 26°N and 41°N, *Geophys. Res. Lett.*, *40*(6), 1159–1164, doi:  
702 10.1002/grl.50233.

703 Montgomery, R. B. (1974), Comments on Seasonal variability of the Florida current, by  
704 Niiler and Richardson, *J. Mar. Res.*, *32*, 533–535.

705 Park, J.-H., and D. R. Watts (2005), Response of the southwestern Japan/East Sea to the  
706 atmospheric pressure, *Deep-Sea Res. II*, *52*, 1671–1683, doi:10.1016/j.dsr2.2003.08.007.

707 Perez, R. C., S. L. Garzoli, C. Meinen, and R. P. Matano (2011), Geostrophic velocity  
708 measurement techniques for the meridional overturning circulation and meridional heat  
709 transport in the South Atlantic, *J. Atmos. and Ocean. Tech.*, *28*(11), 1504–1521, doi:  
710 10.1175/JTECH-D-11-00058.1.

711 Pond, S., and G. Pickard (1983), *Introductory Dynamical Oceanography*, Pergamon in-  
712 ternational library of science, technology, engineering and social studies, Butterworth-  
713 Heinemann.

714 Rahmstorf, S. (1996), On the freshwater forcing and transport of the Atlantic thermoha-  
715 line circulation, *Clim. Dyn.*, *12*, 799–811, doi:10.1007/s003820050144.

716 Rayner, D., J. J.-M. Hirschi, T. Kanzow, W. E. Johns, P. G. Wright, E. Frajka-Williams,  
717 H. L. Bryden, C. S. Meinen, M. O. Baringer, J. Marotzke, L. M. Beal, and S. A.  
718 Cunningham (2011), Monitoring the Atlantic meridional overturning circulation, *Deep-*  
719 *Sea Res. II*, *58*(17–18), 1744–1753, doi:10.1016/j.dsr2.2010.10.056.

720 Richardson, P., and S. Garzoli (2003), Characteristics of intermediate water flow in the  
721 Benguela Current as measured with RAFOS floats, *Deep-Sea Res.*, *50*, 87–118, doi:  
722 10.1016/S0967-0645(02)00380-6.

723 Sabine, C., R. Feely, N. Gruber, R. Key, K. Lee, J. Bullister, R. Wanninkhof, C. Wong,  
724 D. Wallace, B. Tilbrook, et al. (2004), The oceanic sink for anthropogenic CO<sub>2</sub>, *Science*,  
725 *305*, 367–371, doi:10.1126/science.1097403.

726 Shriver, J. F., and H. E. Hurlburt (2000), The effect of upper ocean eddies on the non-  
727 steric contribution to the barotropic mode, *Geophys. Res. Lett.*, *27*, 2713–2716, doi:  
728 10.1029/1999GL011105.

729 Sime, L. C., D. P. Stevens, K. J. Heywood, and K. I. Oliver (2006), A decomposition  
730 of the Atlantic meridional overturning, *J. Phys. Oceanogr.*, *36*(12), 2253–2270, doi:  
731 10.1175/JPO2974.1.

732 Stramma, L., and M. England (1999), On the water masses and mean circulation  
733 of the South Atlantic Ocean, *J. Geophys. Res.*, *104*((C9)), 20,863–20,883, doi:  
734 10.1029/1999JC900139.

735 Sutton, R. T., and D. L. R. Hodson (2005), Atlantic Ocean forcing of North American  
736 and European summer climate, *Science*, *309*, 115–118, doi:10.1126/science.1109496.

737 Thacker, W. C. (2008), Estimating salinity between 25° and 45°S in the At-  
738 lantic ocean using local regression, *J. Atmos. Ocean. Tech.*, *25*, 114–130, doi:  
739 10.1175/2007JTECHO530.1.

740 Timmermann, A., Y. Okumura, S.-I. An, A. Clement, B. Dong, E. Guilyardi, A. Hu, J. H.  
741 Jungclaus, M. Renold, T. F. Stocker, R. J. Stouffer, R. Sutton, S.-P. Xie, and J. Yin  
742 (2007), The influence of a weakening of the Atlantic meridional overturning circulation  
743 on ENSO, *J. Climate*, *20*, 4899–4919, doi:10.1175/JCLI4283.1.

744 Treguier, A. M., M. England, S. R. Rintoul, G. Madec, J. L. Sommer, and J.-M. Molines  
745 (2007), Southern Ocean overturning across streamlines in an eddy simulation of the  
746 Antarctic circumpolar current, *Ocean Sci.*, *3*, 491–507, doi:10.5194/os-3-491-2007.

747 Wainer, I., P. Gent, and G. Goni (2000), Annual cycle of the Brazil-Malvinas conflu-  
748 ence region in the National Center for Atmospheric Research climate system model, *J.*  
749 *Geophys. Res.*, *05*((C11)), 26,167–26,177, doi:10.1029/1999JC000134.

750 Weijer, W., W. P. M. D. Ruijter, H. A. Dijkstra, and P. J. van Leeuwen (1999), Impact  
751 of interbasin exchange on the Atlantic overturning circulation, *J. Phys. Oceanogr.*, *29*,  
752 2266–2284.

753 Willis, J., and L.-L. Fu (2008), Combining altimeter and subsurface float data to estimate  
754 the time-averaged circulation in the upper ocean, *J. Geophys. Res.*, *113*(C12), 2156–  
755 2202, doi:10.1029/2007JC004690.

756 Woollings, T., J. M. Gregory, J. G. Pinto, M. Reyers, and D. J. Brayshaw (2012), Re-  
757 sponse of the North Atlantic storm track to climate change shaped by ocean-atmosphere  
758 coupling, *Nat. Geosci.*, *5*, 313–317, doi:10.1038/ngeo1438.

759 Zhang, R., and T. L. Delworth (2006), Impact of Atlantic multidecadal oscillations on  
760 India/Sahel rainfall and Atlantic hurricanes, *Geophys. Res. Lett.*, *33*, L17,712, doi:  
761 10.1029/2006GL026267.

**Table 1.** Bias  $\pm$  RMS error of the AMOC (Sv) and MHT (PW) introduced by each source of error associated with the AX18 XBT transect observational assumptions estimated in the present study. Last column shows the error estimates of *Baringer and Garzoli* [2007], Table 3.

Source	AMOC (Sv) Meridional Heat Transport (PW)		
	Present	Present	B&G
Upper ocean salinity	$-0.3 \pm 2.6$	$0.02 \pm 0.16$	0.03
Deep climatology below 800 m	$0.06 \pm 2.3$	$-0.03 \pm 0.14$	0.15
Mass imbalance	$0.9 \pm 3.8$	$-0.02 \pm 0.06$	0.02
Non-synopticity	$0.2 \pm 4.2$	$0.02 \pm 0.24$	–
Fall rate equation error (2% of depth)	$-0.06 \pm 0.07$	$-0.01 \pm 0.01$	–
Quarterly sampling	$\pm 2.3$	$\pm 0.24$	–
Unresolved western shelf transport	$-0.6 \pm 0.8$	$10^{-8}$	0.01
Unresolved eastern shelf transport	$0.15 \pm 0.4$	$10^{-8}$	0.01
Western Horizontal resolution	$2.8 \pm 3.2$	$0.13 \pm 0.14$	–
Eastern Horizontal resolution	$0.2 \pm 1.2$	$0.02 \pm 0.04$	–
Interior Horizontal resolution	$-0.4 \pm 1.0$	$0.06 \pm 0.07$	–
Western Reference level	$5.5 \pm 7.1$	$0.06 \pm 0.16$	0.05
Eastern Reference level	$3.5 \pm 5.6$	$0.08 \pm 0.21$	0.05

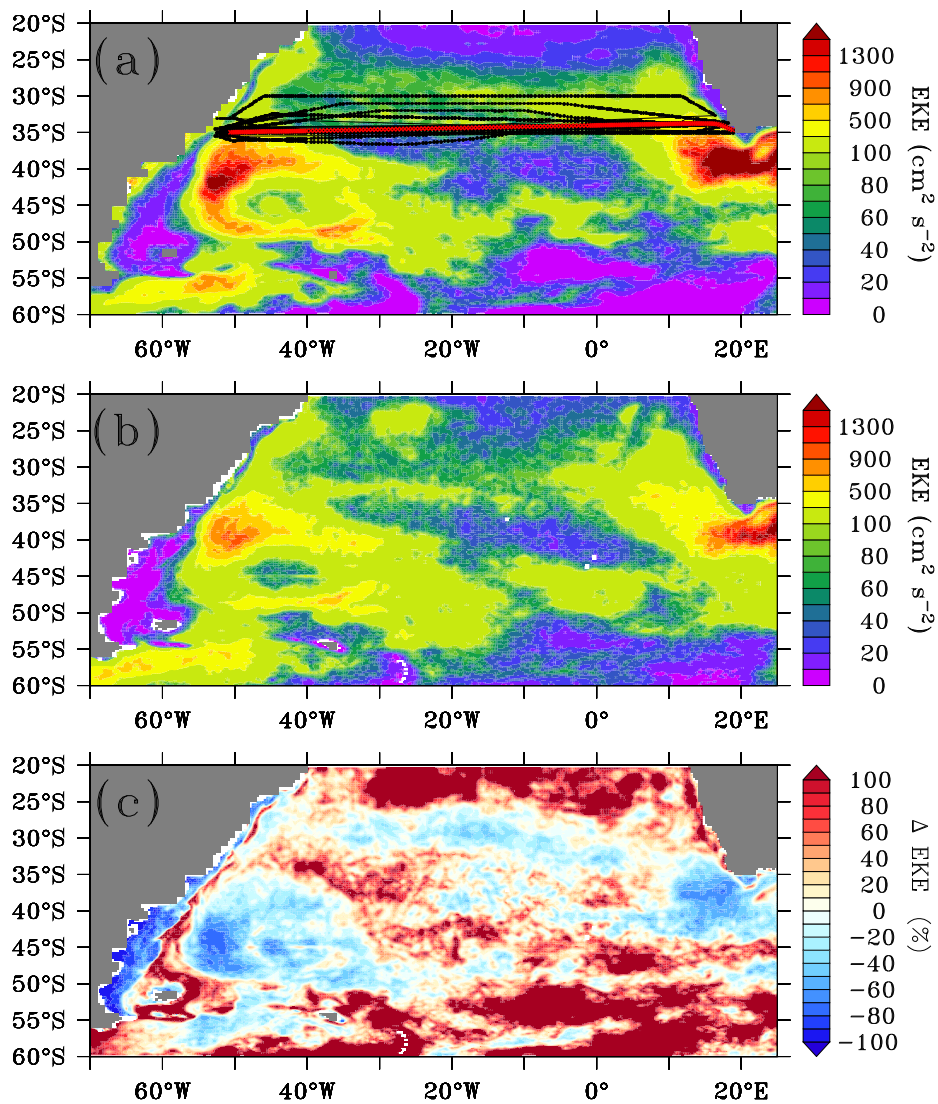


**Figure 1.** Eddy kinetic energy ( $\text{cm}^2 \text{s}^{-2}$ ) calculated from sea level anomalies for the period between 2007 and 2013. (a) AVISO observations, (b) HYCOM model, and (c) HYCOM minus observations. The black lines in Figure 1a are the locations of the 18 selected AX18 transects between 2002 and 2012, overlaid by the mean AX18 transect location in red.



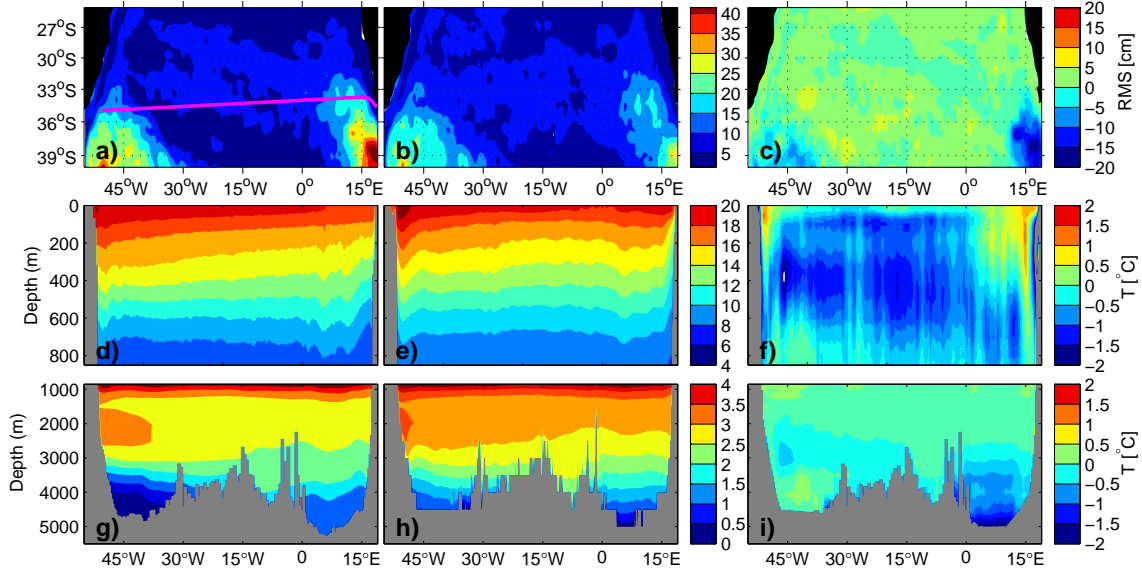


**Figure 2.** (a) – (c) Sea level anomaly (SLA) root-mean-square (RMS) contours (in cm) for: (a) AVISO overlaid by the mean AX18 transect (magenta line); (b) HYCOM/NCODA; (c) HYCOM/NCODA minus AVISO. (d)–(i): Mean temperature sections contours (in °C) for: (d, g) observations, with AX18 data for the upper 850 m (d) and WOA05 for 850 m to bottom (g); (e, h) HYCOM/NCODA model; (f, i) HYCOM/NCODA minus observations.

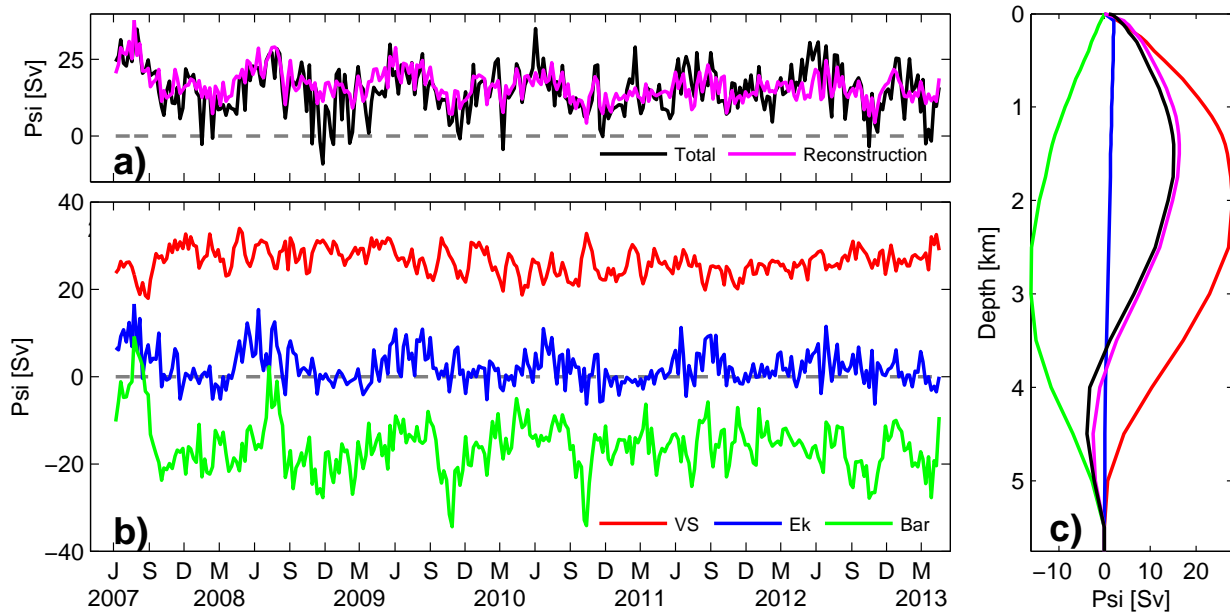


**Figure 3.** (a) Maximum volume transport streamfunction (AMOC) using model velocities (black) and the reconstruction (magenta). (b) AMOC decomposition into vertical shear (red), Ekman (blue), and barotropic (green) components. (c) Time mean meridional transport streamfunction for the model velocities (black), reconstruction (magenta), Ekman (blue), vertical shear (red) and barotropic (green).

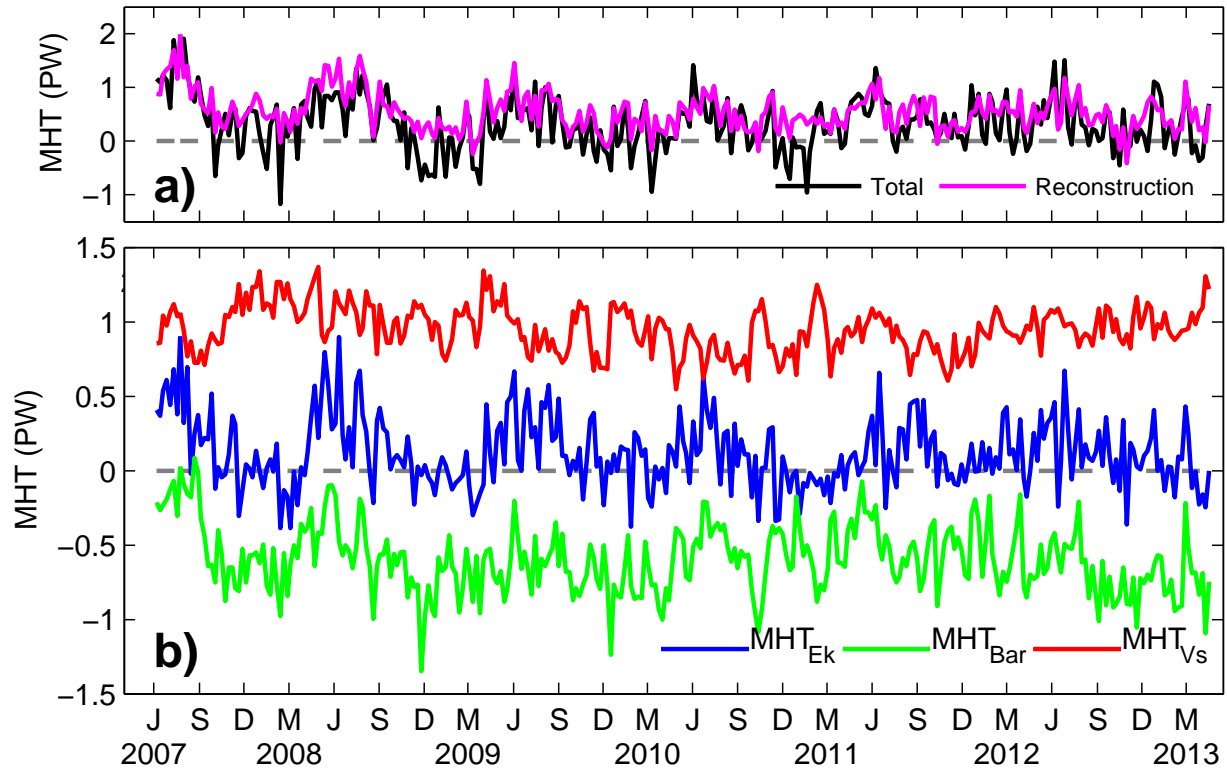


**Figure 4.** (a) Heat transport (MHT in PW) using model velocities (black) and reconstruction (magenta). (b) MHT decomposition into vertical shear (red), Ekman (blue), and barotropic (green) components.

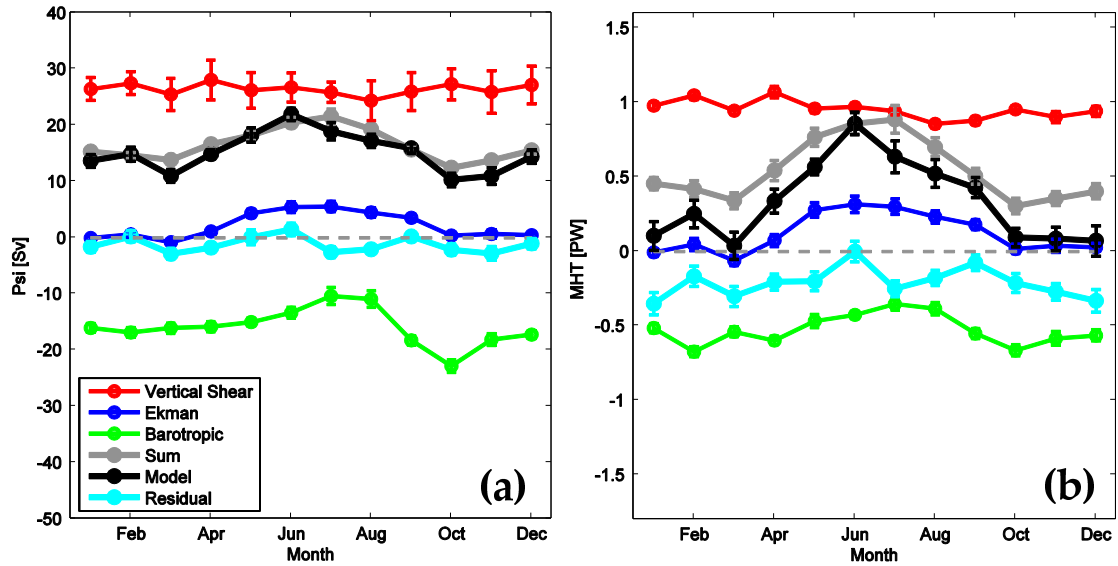


**Figure 5.** Monthly means of the (a) AMOC and (b) MHT components: vertical shear (red), Ekman (blue) and barotropic (green). The level of reference is assumed to be on the ocean bottom using the model bottom velocities as the reference. The sum of the transport components (gray) is comparable to the total transport from the original model velocities (black).

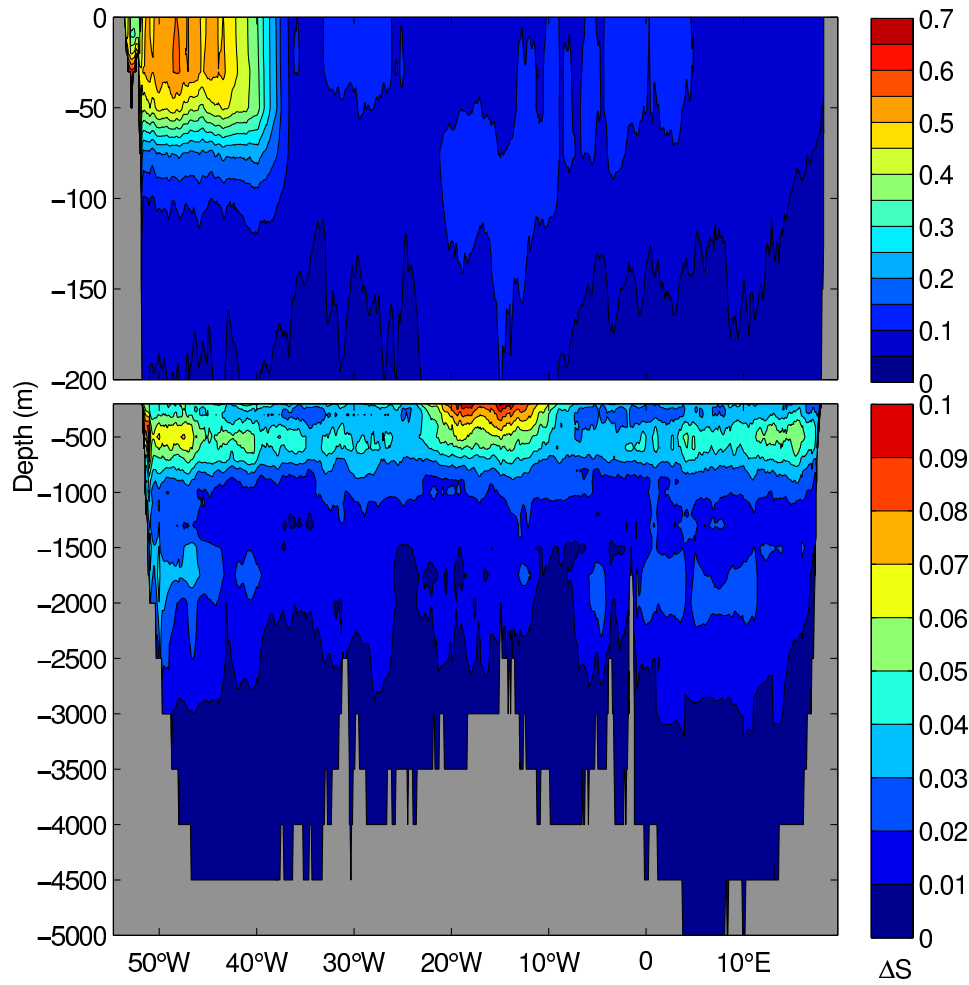


**Figure 6.** RMS error (psu) between the estimated salinity using climatological T-S relationships and the model salinity along the 34.5°S section.

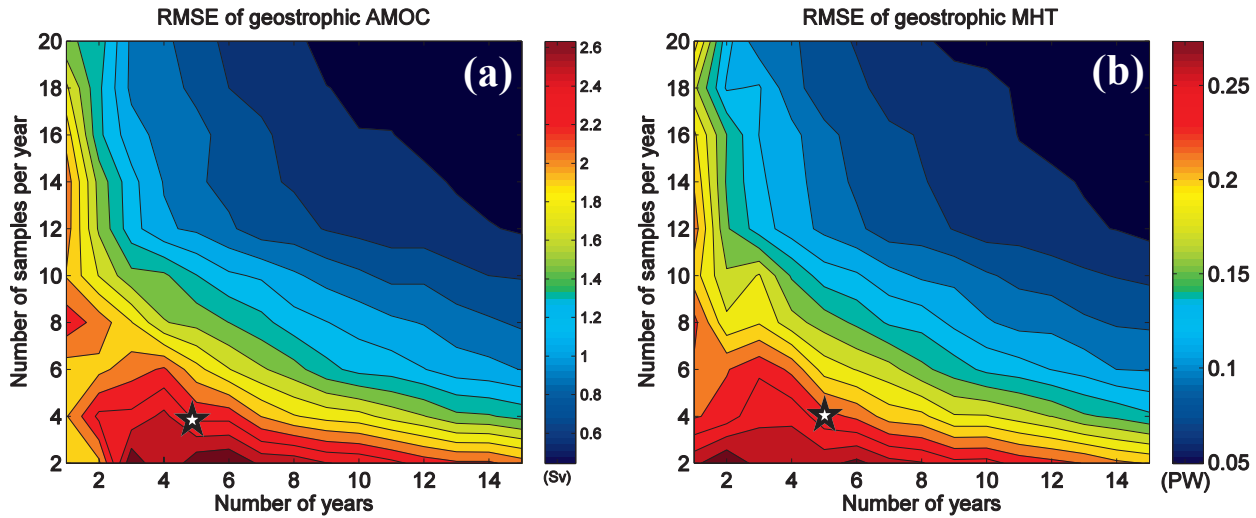


**Figure 7.** RMS error of geostrophic AMOC (a) and MHT (b) associated with different time samplings, i.e., the number of samples per year (y-axis) and the number of year (x-axis). The RMS error is calculated from the difference between the reconstructed time series using a different time sampling and the reconstructed time series using the original model sampling. The number of samples per year is randomly selected, and this process is realized 400 times to average the random realizations. The stars in (a) and (b) correspond to the current location of the AX18 sampling in the time sampling parameter space.

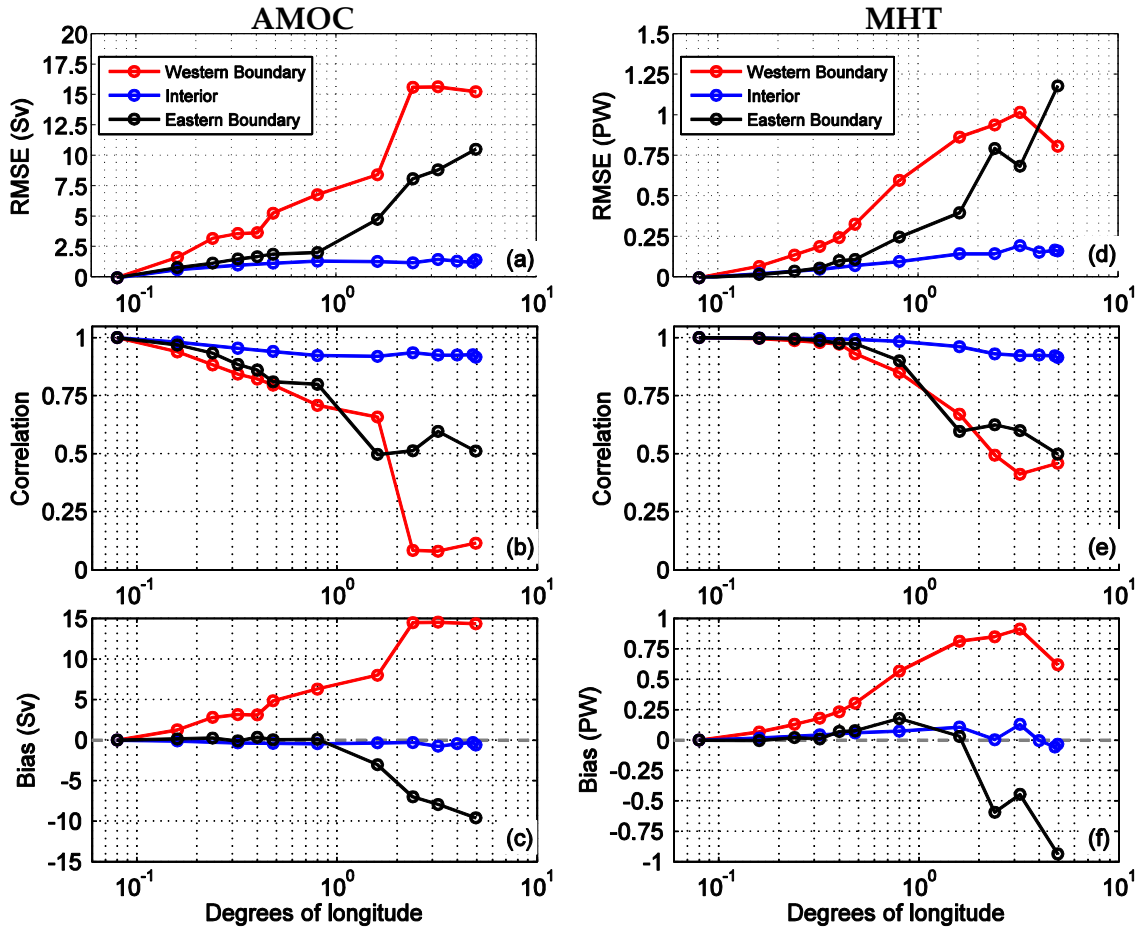
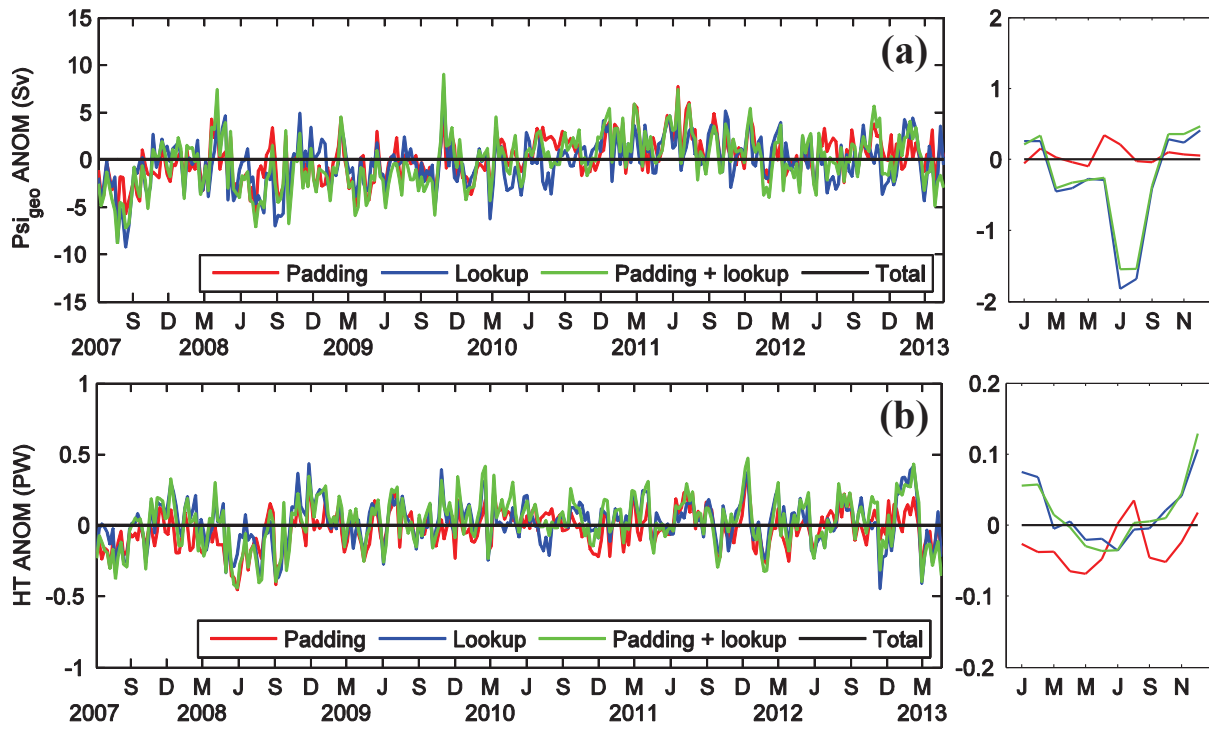
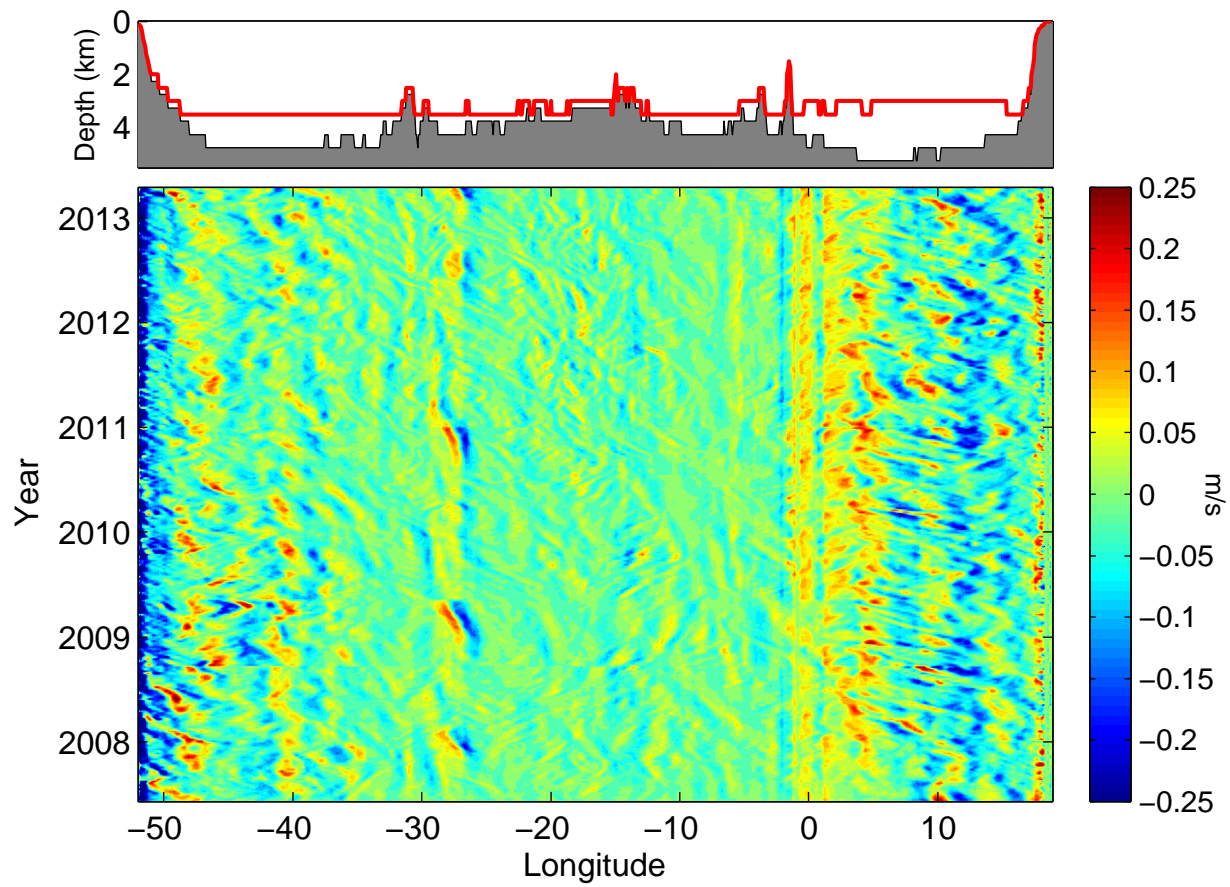


Figure 8. RMS error, correlation, and bias of the AMOC (a, b, c) and MHT (d, e, f) with respect to the simulated longitudinal resolution (in degrees) of the AX18 transect. The transect horizontal resolution varies individually for three regions, western boundary (red), interior (blue) and eastern boundary (black). The x-axis is shown in logarithmic scale.



**Figure 9.** Anomalies relative to the total model field time series of (a) geostrophic AMOC and (b) MHT, and respective monthly averages (right panels). The total field anomalies are defined as having zero value (black), and the colored time series assume a bottom T-S climatology padding (red), salinity inference from lookup table in the top 800 m (blue), padding plus T-S lookup (green), and the total (black).





**Figure 10.** Barotropic velocities at  $34.5^\circ\text{S}$  estimated from the model velocities. The top panel shows the average depth of the  $\sigma_2 = 37.9$  (red line) overlaid on model bathymetry

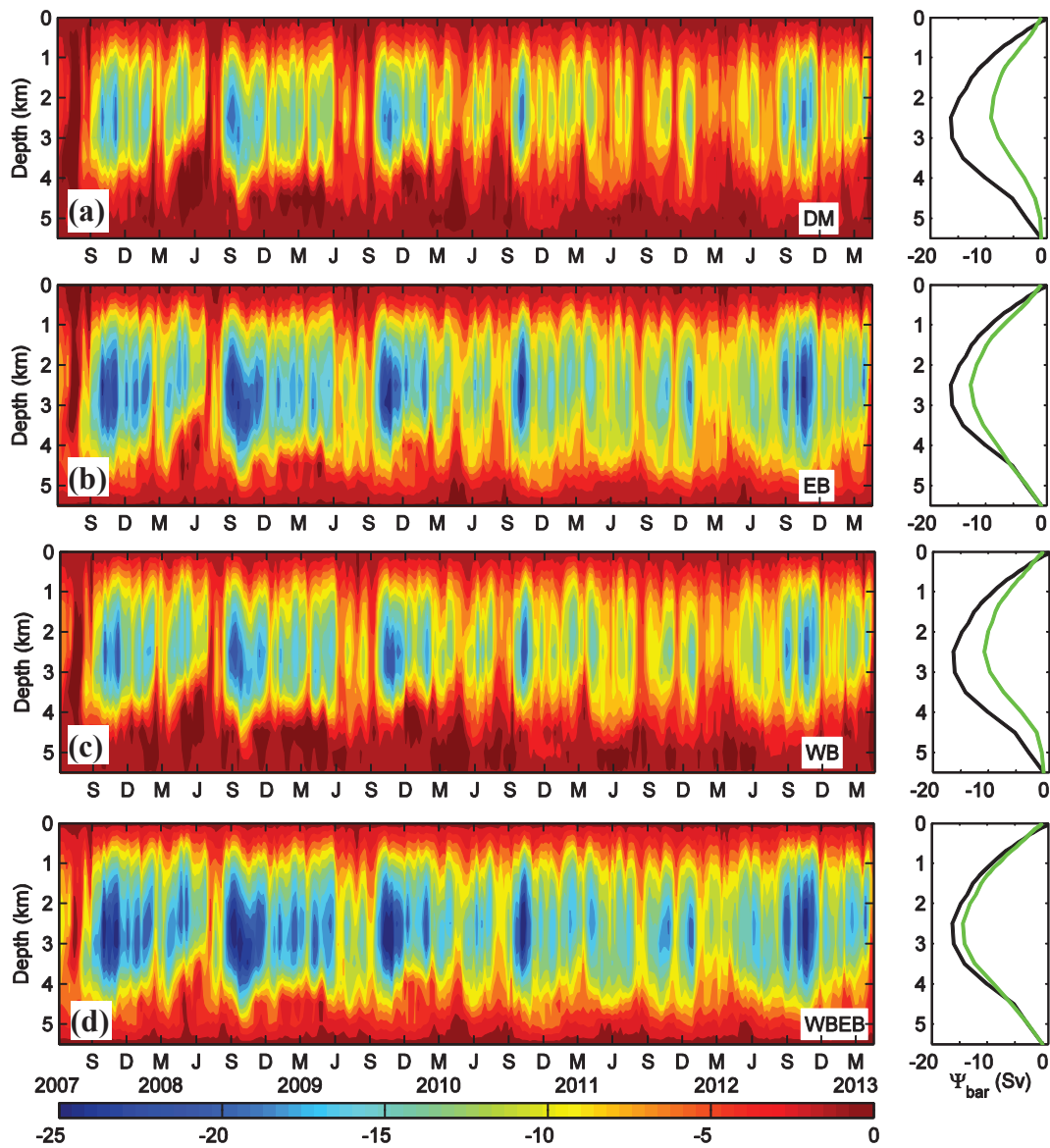


**Figure 11.** Changes in the barotropic streamfunction (Sv) due to the knowledge of a climatological reference velocity at  $\sigma_2 = 37.09$ . (a) Zero reference velocity, (b) eastern boundary, (c) western boundary, and (d) western plus eastern boundaries. Left panels: time evolution of the barotropic streamfunction. Right panels: green line is the time average of the barotropic streamfunction shown on the left panels, and black line is the time average of the original model barotropic streamfunction.

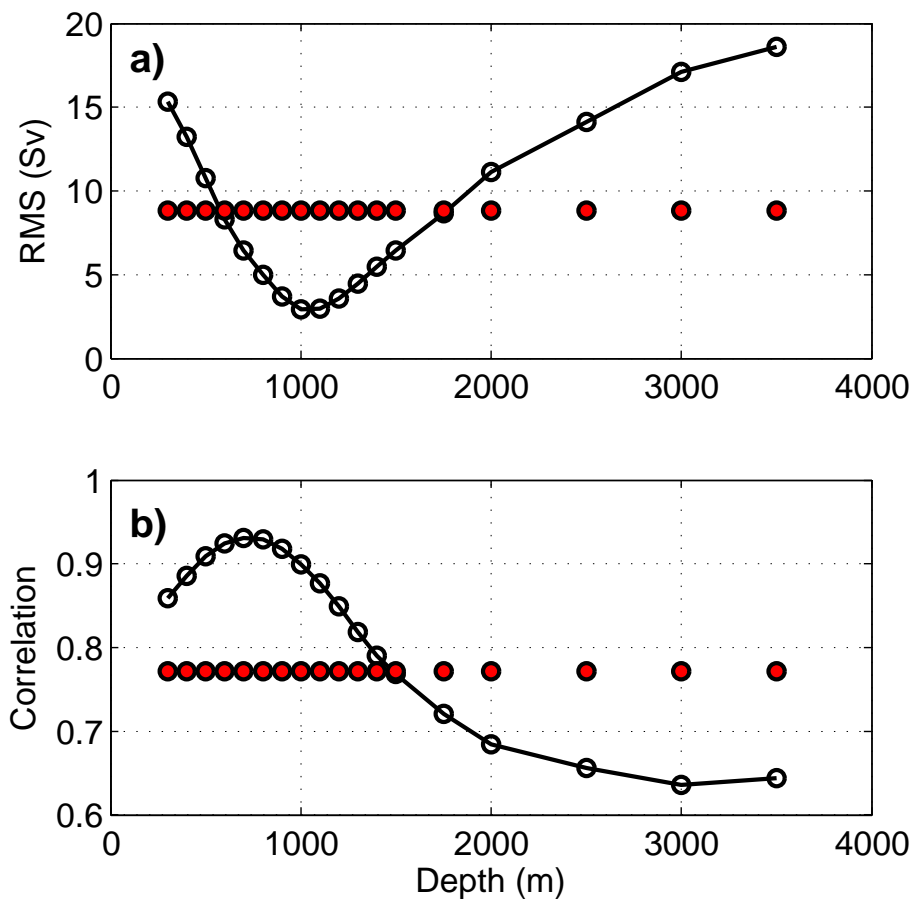


**Figure 12.** a) RMS error and (b) correlation between the barotropic streamfunction strength for the barotropic velocities calculated from the SLH-DH residual with a variable reference level (x-axis) from 300 m to 3500 m depth (line with open dots). Also added for comparison the RMS and correlation of the streamfunction strength for barotropic velocities calculated using a level of no motion at  $\sigma_2 = 37.09 \text{ kg m}^{-3}$  (red dots).